Metal Sulfide Photocatalysts for Hydrogen Generation: A Review of Recent Advances

Zamin Mamiyev [1,*] and Narmina O. Balayeva [1,2,*]

1   Institute of Physics, Chemnitz University of Technology, Reichenhainer Str. 70, 09126 Chemnitz, Germany
2   Center for Materials, Architectures, and Integration of Nanomembranes (MAIN), Chemnitz University of Technology, 09126 Chemnitz, Germany
*   Correspondence: zamin.mamiyev@physik.tu-chemnitz.de (Z.M.); narmina.balayeva@physik.tu-chemnitz.de (N.B.)

Abstract: Metal-sulfide nanostructures have piqued the interest of researchers for decades due to their intriguing optoelectronic properties. Indeed, significant advances and improvements have been made in various fundamental aspects for cutting-edge applications, such as water splitting and hydrogen production. Furthermore, rising demand for low-dimensional materials due to lower material consumption and improved performance due to quantum size effects has spurred research on semiconducting metal sulfides. Consequently, size-controllable nanostructures with diverse morphologies have been fabricated and studied for potential applications. However, the photocatalytic hydrogen evolution rate is still limited mainly by fast recombination rate, poor solar energy utilization and lack of surface-active sites for H_2 reduction. This review will highlight particularly recent findings in metal-sulfide-based photocatalysts for hydrogen evolution reactions, considering the swift development and excellent research in this field. Following a brief overview of fundamental properties, we will explore state-of-the-art strategies for enhancing H_2 generation efficiencies over the pristine, heterostructured and co-catalyzed metal-sulfide photocatalysts.

Keywords: metal sulfide; photocatalyst; water splitting; hydrogen generation; heterogeneous photocatalyst; visible light response; co-catalyst; renewable energy

1. Introduction

Increasing demand for energy consumption triggers a search for new renewable and sustainable energy sources. On the other hand, the emerging climate crisis, such as increased CO_2, NO_2, and other air pollutants, as well as global warming, steadily urges the development of new materials to cope with these problems, alongside providing high alternative energy harvesting and storage capacities. According to the United Nations (UN), energy is the dominant contributor to climate change, providing almost 60 % of total global greenhouse gas emissions [1]. Therefore, investigation of new renewable energy sources has also been included (Goal 7) in the 17 Sustainable Development Goals implemented by the UN [1]. In this regard, as a sustainable energy source, H_2 production has been the focus of increasing fundamental and applied research. In general, hydrogen can be obtained from different sources such as coal or liquid fossil fuels by employing different chemical processes, as summarized in Figure 1. Among all other methods, photocatalytic water splitting has the simplicity of using semiconducting particles in solution with incident sunlight to produce hydrogen and oxygen, as follows.

$$H_2O \; \rightarrow \; H_2 + \frac{1}{2}O_2 \qquad\qquad \delta G^\circ = 238 kJ/mol \qquad\qquad (1)$$

$$PC \; \xrightarrow{\; hv > Eg \;} \; PC^* + h^+ + e^- \qquad\qquad (2)$$

$$\text{Water oxidation:} \quad H_2O + 2h^+ \rightarrow \frac{1}{2}O_2 + 2H^+ \quad (+0.82\ V\ vs\ NHE,\ pH = 7) \quad (3)$$

$$\text{Water reduction:} \quad 2H^+ + 2e^- \rightarrow H_2 \quad (-0.41\ V\ vs\ NHE,\ pH = 7) \quad (4)$$
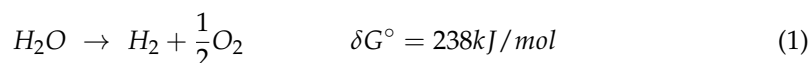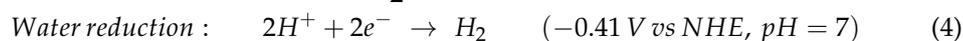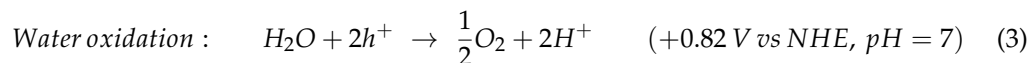
To initiate the oxidation reaction, the valence band (VB) of the photocatalyst must be more positive than the water oxidation potential (+0.82 V vs Normal Hydrogen Electrode (NHE)) (Equation (3)). Whereas, more negative conduction band (CB) in compare to hydrogen evolution potential (−0.41 V vs NHE) is required to drive the reduction reactions (Equation (4)). Ultimately, this process provides a clean and renewable source of hydrogen without producing greenhouse gases or any other harmful products. However, in practice, the simultaneous production of hydrogen and oxygen from water splitting by a single photocatalyst is a tough process since the photocatalyst must fulfill band structure and energy gap criteria. Therefore, combining co-catalysts is a commonly employed strategy for this purpose. In this regard, different catalysts, including homogeneous, heterogeneous, and hybrid, have been developed. Among all others, heterogeneous photocatalysts are known for their high chemical stability in a liquid medium, high recycling or robustness, easier recovery or separation from the reaction medium, nontoxicity, low material, and operational cost, enabling selective product formation, etc.
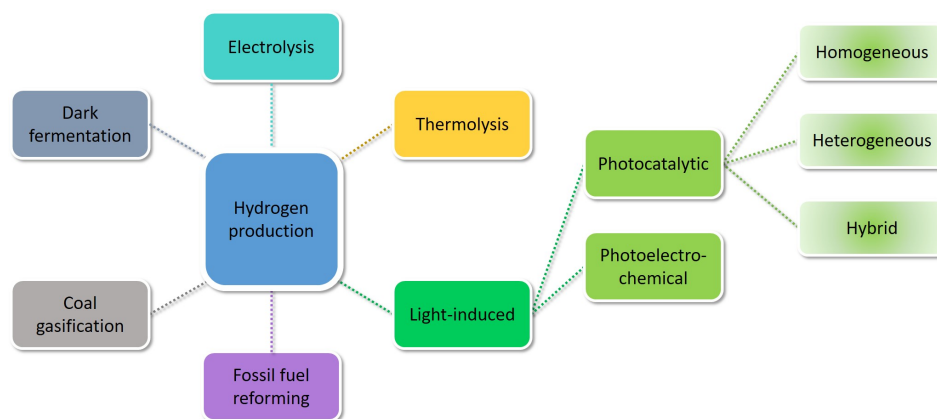
Figure 1. Most used possible routes for hydrogen generation. Currently, the solar-induced hydrogen evolution from water splitting is the most promising approach among others since it is environmentally benign, cost-effective, and offers the potential for high conversion efficiency.

Semiconductor metal sulfides have recently attracted great attention due to their superior physical and chemical properties. Up to nowadays, several binary metal sulfide (MS) compounds (such as PbS, CdS, ZnS, MoS_2, SnS_2, Bi_2S_3, In_2S_3, Cu_2S, NiS/NiS_2, and CoS_2) as well as their derivatives and heterostructures have been intensively employed for versatile purposes [2–7]. In Figure 2, we have summarized the most employed metals as sulfide compounds for photocatalytic hydrogen generation. Most of these compounds have been reported with a remarkable visible light response, sufficient active sites, and appropriate reduction potential of H^+/H_2 as an effective photocatalyst. Moreover, emerging quantum size effects enable further tunability towards fast charge transfer, enhanced excited state lifetime, etc. [8,9]. Thus, in the last decade, tremendous work has been devoted to improving solar hydrogen generation over the MS semiconductor photocatalysts [10–12]. Among other MS materials, ternary sulfides, such as $CuInS_2$, $CuGaS_2$ have been shown to have high selectivity and a high photocatalytic production rate, particularly when coupled to titanium dioxide (TiO_2) [13,14]. Especially, MS with reduced dimensionalities, such as 2D nanosheets, flakes, and anisotropic structures, are in the spotlight of current research. Moreover, the functionalization of low-dimensional MS structures is a growing research toward

high hydrogen production [15]. For example, using metals as dopants or other compounds (i.e., see Figure 2) as co-catalyst is a prominent way of enhancing photocatalytic activity.
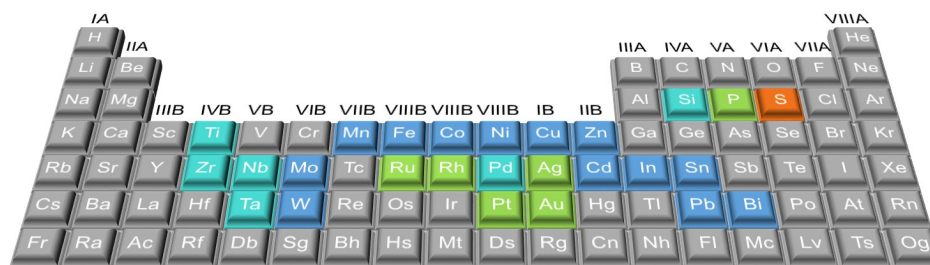

Figure 2. Chemical elements whose sulfide compounds have been widely used in photocatalytic hydrogen generation (blue boxes). Elements employed as dopants (green) and whose oxides or other compounds (cyan) were used to construct heterostructures with metal sulfides for hydrogen evolution are also marked. Please note that lanthanides and actinides are not shown.

Metal sulfide nanostructures have been increasingly employed in hydrogen evolution reactions, especially in the last couple of years [2,16,17]. In this review article, we will discuss the recent breakthrough, mainly in the last two years, regarding nanostructured metal-sulfide photocatalysts for hydrogen evolution as an alternative energy. Following this general introduction, we will briefly discuss the fundamental properties of MS-based photocatalytic systems. This will be followed by discussions on the specific MS systems that have been the focus of very recent research regarding photocatalytic hydrogen production. In each subsection, we will present the possible and most promising routes to photocatalytic enhancement.
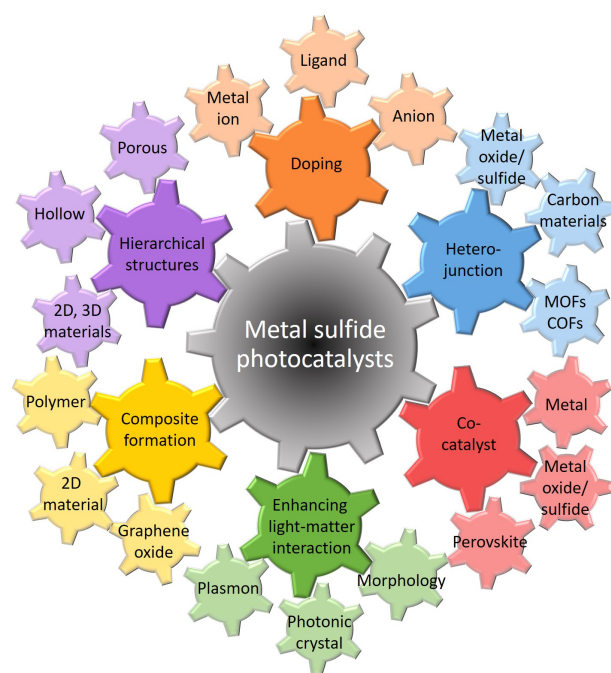
Metal Sulfide Photocatalysts: Design and Mechanisms

As listed in Figure 3, there are specific parameters that are important to improve photocatalytic reaction yield in addition to general environmental and industrial requirements. Certainly, the search for an excellent photocatalyst to meet all requirements has triggered tremendous research resulting in versatile new photocatalysts and photocatalytic reaction routes. Any catalytic process involves fundamental steps like adsorption, interaction, desorption, etc., which determine the overall reaction mechanism, products, and yield [18]. On the other hand, perfect parametrization of these factors enables the design of an effective photocatalyst.
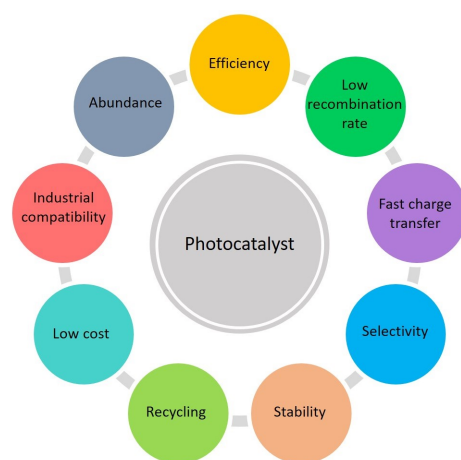
Figure 3. General requirements for designing high-efficiency photocatalysts.

Although photocatalysis based on MS semiconductors is considered an economical, environmentally benign, renewable, and clean technology, the usefulness of these photocatalysts is limited by the low solar energy utilization and the fast recombination of

photoexcited electron-hole pairs. Several strategies have been developed to overcome these intrinsic limitations, that we will discuss in the following parts of this review. General strategies and the most employed combination for the related strategy for metal sulfide-based photocatalysts are listed in Figure 4. Designing new morphologies and decoration of particles are recent trends to enhance the light spectrum absorbed by the semiconducting photocatalysts. For example, hollow structures, porous morphology, nanorods (NRs), 1D nanowires (NWs), 0D quantum dots (QDs), 2D sheets, and layered structures are the focus of current research and development regarding the photocatalytic hydrogen production. In this regard, mesoporous structures have been shown to facilitate the transport of reactant and reaction products [19]. Besides that, the porous medium improves sunlight absorption due to multiple reflections of light waves in porous networks [20]. Moreover, porous structures possess a high Brunauer-Emmett-Teller (BET) surface area with more active sites, which facilitates the photocatalytic reaction. Besides enhancing solar energy utilization, photocatalytic enhancement also requires improved separation efficiency of photogenerated charge carriers, which can also be achieved by designing appropriate architectures with the help of low-dimensional nanostructures. According to Tang et al., the charge carrier recombination on the surface of semiconducting photoatalyst is $\sim 2 \times 10^7$ fs, which is three orders of magnitude faster than chemical oxidation/reduction reactions (10^{10}–10^{11} fs) [21]. Therefore, single component photocatalysts are frequently ineffective for H_2 generation reaction. In order to alleviate this shortcoming combining metal sulfides with metal oxide co-catalsts has been demonstrated as a powerful approach. This type of composite photocatalyst reduces charge carrier recombination of MS while also broadening the light absorption range of wide band gap metal oxide.

Figure 4. The most frequently employed strategies and representative components for enhancing hydrogen production over the metal sulfide photocatalysts. The figure was designed in accordance with the recent literature discussed in this review.

　　Notably, size reduction improves the touching surface areas and strengthens the inter-particle interactions, facilitating rapid photoexcited charge transport. Moreover, emerging quantum size effects bring about strong electronic interaction developing fast charge transfer. Also, the formed discrete states and trap states at quantum particles further improve the electron-hole separation, leading to a reduced charge recombination rate [6,22–24]. The robustness and recycling cycles are being improved with more rugged materials and pro-

tective surface coatings. Other than these, coupling the MS photocatalysts with plasmonic metallic structures has been intensively investigated over the last few years. When noble metal (e.g., Au, Ag, Pt) NPs are attached to the semiconductor nanostructures, the photo-generated electrons in the CB of semiconductor can transfer to the adjacent metals due to their lower Fermi energy level.

The Schottky barrier formed at the metal/semiconductor interface promote electron/hole separation in photocatalysis, while the metal act as electron sinks. The photoinduced the electrons in noble metals and holes in the VB of semiconductor participate in subsequent redox reactions. The whole process increases charge carrier lifetime and improves photocatalytic activity. The unique localized surface plasmon resonance (LSPR) of noble metal NPs can boost photocatalytic activity by increasing incoming photon absorption. Furthermore, the facile tunability of LSPR (i.e., by adjusting size and shape) allows for a broad spectrum of light absorption.

Another useful parameter to achieve higher hydrogen evolution rate (HER) is a high active crystallographic orientation or facet. In this context, zinc-blende CdS nanocubes with a well-controlled charge flow and selective transfer of photogenerated electrons and holes to the (111) and (100) facets, respectively, demonstrated better charge carrier separation and significant photocatalytic H_2 production by water splitting [25].

Usual high-performance photocatalytic materials with large band gaps, such as TiO_2, ZnO, and others, absorb light exclusively in the near-UV region ($\lambda = 400$ nm). Most low-bandgap photocatalysts, such as CdS, on the other hand, retain photoactivity for short time due to photocorrosion, which occurs when the sulfur ions are attacked by photogenerated holes and oxidized to elemental sulfur. Also, early researches on metal chalcogenide photocatalysts revealed that hole transport plays a limiting role in these nanostructures. To tackle this shortcoming, the isolation of photoinduced holes from the reaction site has been suggested [26]. For example, in Pt/CdS-CdSe heterostructures, the holes are confined to the CdSe, whereas the delocalized electrons are transferred to the Pt tip. This was due to larger VB edge of CdSe than CdS, and consequently resulted in significant photocatalytic activity [11]. Compared to photocatalysts made up of only one type of semiconductor, heterojunction structures often possess altered band alignment at the interface, enhancing carrier separation and limiting carrier recombination for enhanced photocatalytic activity. Sulfide atoms near metal ions in typical metal sulfides potentially act as a catalytic site for the attachment and detachment of H atoms. Therefore, the increased number of sulfur sites is another parameter for enhancing photocatalytic activity. Noteworthy, compared to crystalline metal sulfides, amorphous metal sulfides often exhibit more unsaturated sulfur atoms with excessive chemical reactivity, functioning as active sites for H_2 production. In Figure 5, the band gap energy with respect to the water oxidation and reduction potential is summarized for representative semiconductor metal sulfides.
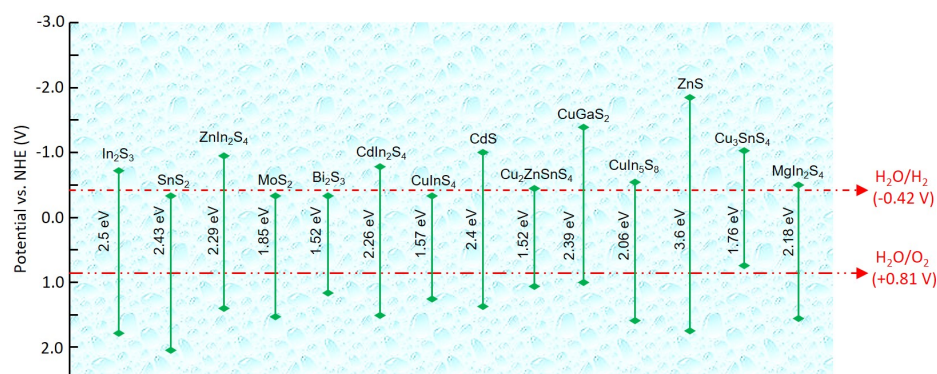

Figure 5. The band gap and band positions of the selected MS semiconductors, along with the needed oxidation and redox potential for water splitting. Data obtained from, In_2S_3 [27], SnS_2 [28], $ZnIn_2S_4$ [29], MoS_2 [30], Bi_2S_3 [31], $CdIn_2S_4$ [32], $CuInS_2$ [33], CdS [34], Cu_2ZnSnS_4 [35], $CuGaS_2$ [36], $CuIn_5S_8$ [37], ZnS [38], Cu_3SnS_4 [39], $MgIn_2S_4$ [40].

Morphological modifications and the construction of heterojunction photocatalysts are the two most employed techniques to increase the performance of photocatalytic hydrogen evolution significantly. The close distance between the two nanosheet subunits induces a strong interaction, facilitating the separation and transfer of charge carriers. In this regard, a reverse cation exchange-mediated and a $Cu_{2-x}S$ nanocube template-assisted growth strategy for fabricating hollow multinary metal sulfide was reported recently [41]. Thus, it was found that in contrast to the typical cation exchange mechanism mediated by the metal sulfide constant, the presence of tri-n-butylphosphine (TBP) can reverse cation exchange to produce a series of hollow metal sulfides. Various hollow metal sulfide cubic NSs were demonstrated using this method, including binary compounds (CdS, ZnS, Ag_2S, PbS, SnS), ternary compounds ($CuInS_2$, $Zn_xCd_{1-x}S$), and quaternary compounds (single-atom platinum attached $Zn_xCd_{1-x}S$; $Zn_xCd_{1-x}S$-Pt_1). Also, a light-induced deposition approach to precisely load nickel sulfide nanodots onto the surface of g-C_2N_2 resulted in both enhanced photocatalytic hydrogen evolution and oxygen reduction performances over composite photocatalysts [42]. In general, as demonstrated in Equations (1)–(4), photocatalytic water splitting involves three significant steps: the generation of electron-hole pairs by photon absorption, the separation of electron-hole pairs and migration to the photocatalyst surface, and the splitting of water molecules via charge carriers on the photocatalyst surface.

One should emphasize that depending on the selected co-catalyst or heterojunction, the reaction pathway follows different routes, which are mainly dictated by the chemical potential of the components. In this regard, different routes have been reported in the literature, which are also valid for metal sulfide photocatalysts. The most pronounced photocatalytic reaction types are illustrated in Figure 6. In type-I heterojunction, a built-in electric field is established by a photogenerated charge carrier inside the large band gap semiconductor before it is transmitted into the narrower band gap semiconductors; thus, electron-hole pairs cannot be spatially separated. On the contrary, in the type-II heterojunctions between two semiconductors, rapid generation of a built-in electric field induces a prolonged lifetime of photogenerated charge carriers. Therefore, in engineering a photocatalytic system for enhanced charge carrier separation in heterojunction, facilitating a suitable type-II interfacial contact with effective carrier migration pathways is critical (i.e., see Figure 6). For instance, Liu et al. synthesized a type-II hexagonal cadmium sulfide (CdS)/molybdenum disulfide (MoS_2) heterostructure for photocatalytic hydrogen production [43]. The synergetic enhancement in the charge dynamics of the excited carriers on the heterostructure interface of the CdS on the MoS_2 film was investigated by transient absorption spectroscopy. Type-III heterostructures are called Van der Waals broken band gap heterojunctions, which are less investigated in applying two-dimensional (2D) photocatalytic materials for hydrogen production. That is because the photogenerated charge carriers are not synergistically coupled; thus, electron-hole pairs exhibit a fast decay. In the S-scheme heterojunction, strong photogenerated holes and electrons in the valence and conduction bands, respectively, participate in the redox reactions. Meanwhile, weak photogenerated carriers are recombined by the internal electric field and Coulomb gravity. As a result, more efficient electrons for photocatalytic hydrogen reduction can be used [44]. In all-solid- state Z-scheme photocatalysts, NPs such as noble and transition metals (Ag, Au, Rh, Ru, Cu, Pt, etc.) are used as electron conductors/mediators between two SCs due to their strong reduction ability. This type of heterojunction has been studied extensively over the last decade with different combinations of the SCs after the pioneering work of the anisotropic CdS-Au-TiO_2 nano junction SCs [45]. The direct Z-scheme photocatalytic process, which involves two steps of photoexcitation, mimics the natural photosynthesis process, which also requires the spatial isolation of photogenerated electrons and holes. By pooling photogenerated electrons, an electron-rich region forms in the CB of SC I, and by pooling photogenerated holes, a hole-rich region generates in the VB of SC II, which reduces bulk electron-hole recombination in this type of heterojunction. Meanwhile,

the photogenerated electrons in the CB of PC II and holes in the VB of PC I with less redox power recombine.
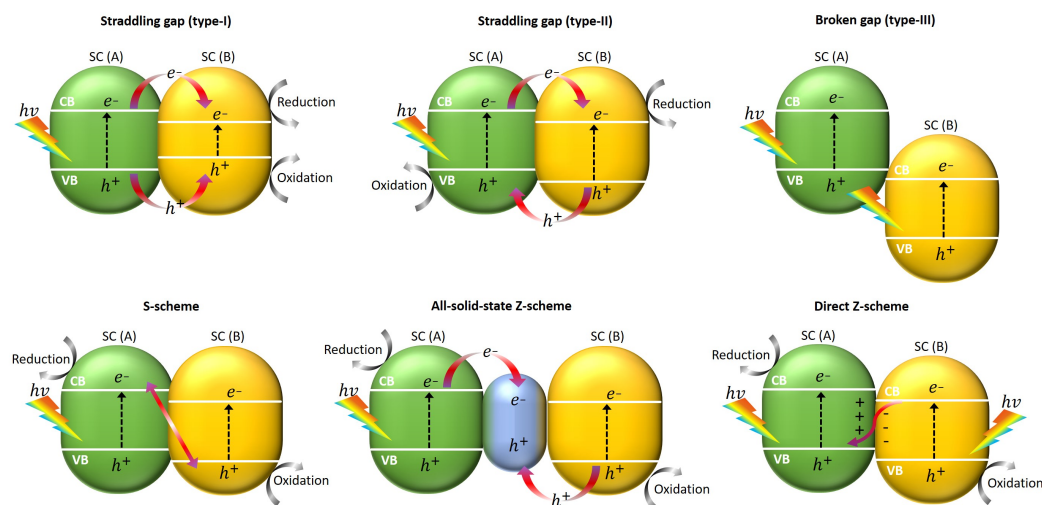
Figure 6. Schematic illustration of the most frequently reported charge transfer mechanisms for any photocatalytic systems. SC(A) and SC(B) stand for the two different semiconductor components of the corresponding photocatalyst.

2. Hydrogen Generation as an Energy Material

2.1. Binary Metal Sulfide Compounds

Semiconductors, with a large band gap energy, can only be activated under UV irradiation, which limits their efficiency in terms of using a narrow light spectrum. CdS, with its energy level of CB being more negative than the potential of water reduction, is one of the most suitable semiconductors for water splitting by utilizing visible-light irradiation [46–51]. However, a general drawback, photocorrosion, is also related to CdS. Thus, sulfur anions (S^{2-}) tend to be oxidized easier than water at the surface of the anode. Ultimately, hole scavengers, which can easily provide electrons reacting with holes such as alcohol, S^{2-}, SO_3^{2-}, etc., are required to react with h^+ to neutralize the reaction for continuous H_2 evolution. Thus, introducing CdS as the main photocatalyst or as a component in different chemical compounds is one of the effective ways to improve its usefulness for water splitting. For example, it is known that nickel boride (Ni_xB), which is a well-known low-cost photocatalyst, suffers from the weakening of atomic H adsorption on Ni active site by the electron transfer from B to Ni atoms, which causes the inhibition of H_2 evolution. In order to enhance the photocatalytic H_2 generation over CdS, Zhang et al. have prepared a Ni_xPB-rGO/CdS hetero-photocatalyst, where the Ni_xB was doped by metalloid P to enhance its H adsorption ability [52]. The 8-10 nm Ni_xPB are loaded on reduced graphene oxide (rGO) and coupled with CdS nanoparticles. The as-synthesized photocatalysts exhibited H_2 evolution rate of 5.79 mmol h^{-1} g^{-1}, being 1.8 and 9.9 times higher than the Ni_xB-rGO/CdS and rGO/CdS photocatalysts, respectively. Similarly, CdS@Ni_2P was prepared by a simple hydrothermal method followed by in situ photodeposition [53]. The highest photocatalytic hydrogen production rate achieved with this composite was 287 µmol g^{-1} h^{-1}, that is ∼98.3 times that of pristine CdS. The higher activity was related to the effective interface between the Ni_2P co-catalyst and CdS nanorods, which leads to better separation and transport of photogenerated electrons.

For solar-driven water splitting, $NiWO_4$/CdS nanosheets-on-nanorods direct Z-Scheme heterostructure was developed by using a facile in-situ approach (see Figure 6 for Z-scheme photocatalysts) [54]. The fabricated $NiWO_4$/CdS heterostructure photocatalysts showed a H_2 evolution rate of 26.43 mmol g^{-1} h^{-1}, which is 75 times higher than that of bare CdS. It was shown that the nanostructures with multiple active sites, intimate

contact interface, and improved charge separation rate are responsible for the enhanced photocatalytic performance.

Another strategy to improve the photocatalytic activity of semiconductor materials is employing metalloid compounds, which form a Schottky junction with the semiconductor at the heterogeneous interface. In this regard, tungsten nitride (WN) nanosheets, which have excellent electron conductivity, were employed as a new noble-metal-free co-catalyst to improve the H_2 evolution performance of CdS NPs via the one-pot solvothermal method [55]. The H_2 production rate of the WN/CdS composite photocatalyst under visible light irradiation reached 24.13 mmol g^{-1} h^{-1}, which is 9.28 times that of pure CdS NPs. Similarly, P-rich platinum diphosphide (PtP_2) nanodots were used to improve the photoactivity of CdS by a facile phytic acid-assisted pyrolysis [56]. The obtained PtP_2@C/CdS(10 wt%) photocatalyst presents an optimum H_2 evolution rate of 9.76 mmol g^{-1} h^{-1} with apparent quantum efficiency (AQE) of 41.67% (420 nm), which is 2.2 and 34.8 times higher than that of Pt@C/CdS and clean CdS, respectively. It was found that the electron-enriched P-rich PtP_2 can serve as the effective H-proton adsorption active site to enhance the photocatalytic activity greatly.

As discussed previously, designing porous photocatalysts is one of the major trends for HER enhancement. In this perspective, three-dimensional ordered macroporous (3DOM) structures have received increased attention because their open interconnected hierarchical macroporous architecture facilitates the transport and diffusion processes of species, leading to enhanced photocatalytic enhancement. Furthermore, the regularly ordered structure of 3DOM results in photon band gaps and the slow photon effect of photonic crystals, which can significantly improve the photoinduced carriers and boost photocatalytic activity. Additionally, changes to the pore walls typically do not modify the 3DOM structure, making it easy to build efficient photocatalysts with diverse materials. In this regard, recently, a CdS photocatalyst with a 3DOM structure using polymethylmethacrylate as a template was reported [57]. In line with the expectations, photocatalytic H_2 evolution rate of 20.1 mmol g^{-1} h^{-1} was achieved, which is remarkably improved in comparison with the CdS NPs. Moreover, as shown in Figure 7f, HER was further enhanced by loading Pt metal. The schematic view of the preparation procedure, corresponding structural characterization, HER results, and proposed H_2 evolution mechanism over CdS 3DOM photonic crystals are summarized in Figure 7.
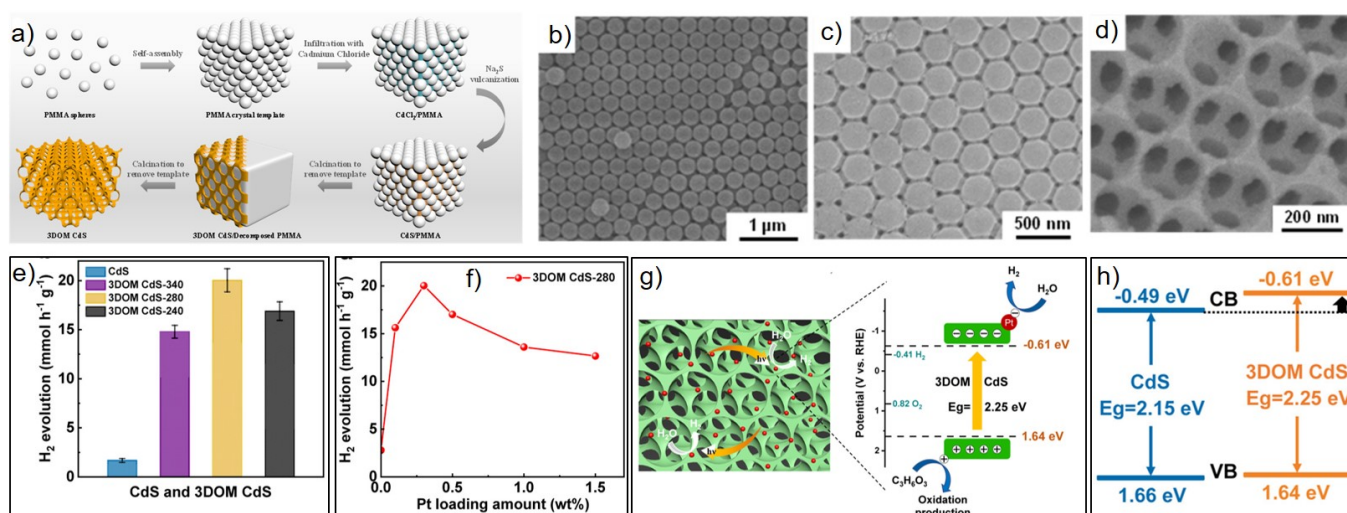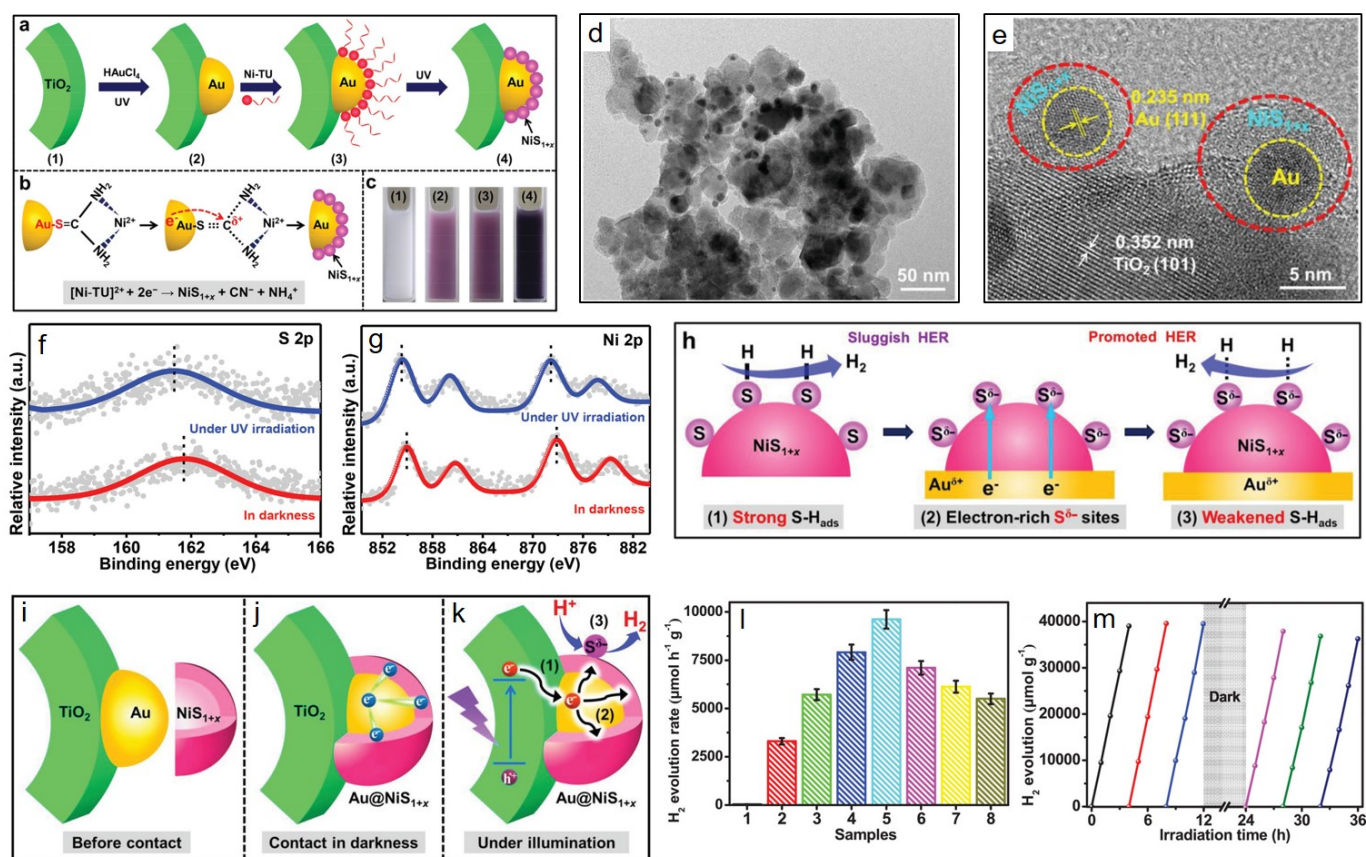

Figure 7. (**a**) Schematic illustration of the overall synthetic strategy of 3D ordered macroporous (3DOM) CdS. (**b**) PMMA crystal template. (**c**) PMMA/CdS. (**d**) 3DOM CdS. (**e**) HER efficiency over the CdS NPs and 3DOM CdS with 0.3 wt% Pt loading. (**f**) Efficiency of HER over the 3DOM CdS-280 with different Pt loadings. (**g**) Schematic illustration of 3DOM CdS for photocatalytic H_2 production. (**h**) Schematic illustration of the band gap states of CdS NPs and 3DOM CdS. [57] Copyright 2022, American Chemical Society

Also, a hybrid heterojunction consisting of CdS NPs and structurally defined graphene nanoribbons (GNRs) was reported with an enhanced HER [58]. Through photocurrent, electrochemical impedance, steady-state photoluminescence, and time-resolved fluorescence decay spectroscopy, it was revealed that the CdS/GNR heterojunction could efficiently reduce the photoexcited electron-hole pair recombination. Notably, the CdS/GNR hybrid displayed H_2 evolution rate up to 22.4 mmol g^{-1} h^{-1} under Vis-light irradiation ($\lambda = 420$ nm), which is much greater than that of individual CdS and GNRs. Lei et al. employed the facile solid-liquid mixing method to load CdS onto WC [59]. 3 wt% WC-loaded CdS photocatalyst (CdS/WC) exhibiting the highest HER of 9180 µmol g^{-1} h^{-1} with an AQE of 14.3% at 420 nm. Thus, incorporating WC improves the light absorption capability of CdS NPs. Moreover, a more conductive WC provides a fast electron transfer channel and water reduction site, which enhances the spatial photogenerated charge separation while facilitating the H_2 production.

Alongside metal sulfide-based heterostructures, doping the metal sulfides with metals is also a promising trend toward photocatalytic H_2 generation. For example, Ni_xCd_yS composite photocatalysts possessing porous structure, large specific surface, and highly dispersed metal active sites were synthesized using Ni-doped CdS [60]. The fabricated Ni_xCd_yS photocatalysts showed three times higher H_2 yield (i.e., 8.45 mmol g^{-1} h^{-1}) than the CdS. NiS_{1+x} compounds have recently gained interest as low-cost transition-metal chalcogenides for effective photocatalytic H_2 evolution [61,62]. Co-catalyst-free NiS (α and β phases) nanostructures for photocatalytic H_2 generation was reported [63]. Unfortunately, due to the limited number of exposed sulfur sites and their strong interaction with adsorbed hydrogen atoms, these materials are ineffective for H_2 generation. To overcome these limitations, Gao et al. developed a nanostructured core-shell $Au@NiS_{1+x}$ co-catalyst and adjoined with TiO_2 by employing a two-step route [61]. The synthetic route for producing the core shell structures, as well as their characterisation, is shown in Figure 8a–g. The optimized $TiO_2/Au@NiS_{1+x}$(1.7:1.3) exhibited high HER of 9616 µmol g^{-1} h^{-1} with an AQE of 46.0% at 365 nm, which is 2.9 and 1.7 times higher than the HER obtained for the TiO_2/NiS_{1+x} and TiO_2/Au photocatalysts, respectively. By XPS studies complemented by DFT calculations, it was shown that the conductive-electrons of Au can transfer to sulfur-enriched NiS_{1+x} resulting in electron-enriched active sulfur centers. This weakens the strong bonds between sulfur and adsorbed hydrogen atoms and facilitates desorption of adsorbed hydrogen for rapid hydrogen formation. Figure 8 depicts the photocatalytic performance as well as the associated charge transfer process.

Besides the aforementioned compounds, Fe_3S_4 (greigite), which is a ferromagnetic material, has also recently been extensively investigated for energy applications, including high-energy batteries, electrochemical hydrogen storage because of its low-cost, and environmental benignity and natural abundance. In addition to the sulfur ions acting as H-adsorption/desorption sites, the mixed Fe^{2+}/Fe^{3+} valence states in the inverse spinel structure also endow this material with relatively higher electric conductivity than the FeS and FeS_2, which makes it more suitable photocatalysts for H_2 generation. However, Fe_3S_4 crystal possesses inappropriate surface adsorption energy for H atoms, which can be altered by doping with additional metal atoms. In this regard, Fe_3S_4 nanorods were derived from a metal-organic framework by a facile method and its HER capability was further enhanced by Ni doping [64]. Thus, the organic dye (eosin-Y) sensitized, 1%Ni-doped Fe_3S_4 nanorods showed remarkably improved H_2 generation rate of 3240 µmol g^{-1} h^{-1} with an AQE of 12% under $\lambda = 500$ nm. Due to its unique localized surface plasmon resonance in the near-IR region, the $Cu_{2-x}S$ has showeds substantial promise in the field of broad-spectrum driven photocatalyst engineering. Nonetheless, inefficient carrier separation and severe photocorrosion limit its practical uses.

Figure 8. Schematic illustration of the synthesis procedure of the core-shell Au@NiS$_{1+x}$ combined TiO$_2$ photocatalyst (**a**) and the formation mechanism of NiS$_{1+x}$ on Au surface (**b**). (**c**) shows the corresponding photographs for (1) TiO$_2$, (2) TiO$_2$/Au, (3) TiO$_2$/Au@Ni-TU (TU stands for thiourea), and (4) TiO$_2$/Au@NiS$_{1+x}$. (**d**) TEM and (**e**) HRTEM images of the TiO$_2$/Au@NiS$_{1+x}$(1.7:1.3) photocatalyst. (**h**) Schematic illustration for activating H-adsorbed S on Au-mediated NiS$_{1+x}$ by forming electron-enriched active S sites. In situ irradiated XPS spectra of S 2p (**f**) and Ni 2p (**g**) for TiO$_2$/Au@NiS$_{1+x}$ in dark and under UV-light illumination. (**h**) Schematic view of charge transfer within TiO$_2$/Au@NiS$_{1+x}$: (**i**) before contact, (**j**) contact in the dark and (**k**) during UV irradiation: the (1) photoelectron trapping by the Au mediator, (2) photoelectron transfer from Au to NiS$_{1+x}$, and (3) fast H$_2$ evolution on the electron-enriched S active sites of Au@NiS$_{1+x}$ co-catalyst. (**l**) Photocatalytic HER over (1) TiO$_2$, (2) TiO$_2$/NiS$_{1+x}$, (3) TiO$_2$/Au@NiS$_{1+x}$(2.5:0.5), (4) TiO$_2$/Au@NiS$_{1+x}$(2:1), (5) TiO$_2$/Au@NiS$_{1+x}$(1.7:1.3), (6) TiO$_2$/Au@NiS$_{1+x}$(1.5:1.5), (7) TiO$_2$/Au@NiS$_{1+x}$(1:2), and (8) TiO$_2$/Au. (**m**) Recycling test for hydrogen evolution over the TiO$_2$/Au@NiS$_{1+x}$(1.7:1.3) photocatalyst. [61] Copyright 2022, Wiley-VCH.

Recently, multinary compounds based on Cu$_x$S synthesized by a facile colloidal method were also reported as effective photocatalysts for the H$_x$ evolution [65]. There, the authors incorporated Ni, Co, Mn, Zn metals to enhance activity of Cu$_x$S and reaction rates of H$_x$ generation was found in the order of Ni:Cu$_x$S > Co:Cu$_x$S > Mn:Cu$_x$S > Zn:Cu$_x$S as 4.0, 1.2, 0.9 and 0.7 mmol g^{-1} h^{-1}, respectively. The higher efficiency of the Ni-doped Cu$_x$S nanorods can be attributed to the effective charge carrier separation and fast transport similar to the Ni-CdS, as discussed above. Molybdenum disulfide (MoS$_2$) is another potential low-cost photocatalyst for hydrogen production reactions. According to the previous studies, the active sites for the catalytic reaction are mainly associated with the edge sites of 2D-layered MoS$_2$, however, the basal plane shows poor activity toward catalytic reactions. Thus, activating the basal planes is another route for enhancing its HER. In this regard, Ni-doping and exfoliation were reported to convert the in-plane sites to active edge sites [66]. Furthermore, the activated MoS$_2$ was utilized for enhancing

the photocatalytic activity of CdS toward H_2 production. The resulting Ni-MoS$_2$/CdS nanocomposite photocatalysts showed a H_2 evolution rate of 249 mmol h^{-1} g^{-1}, which is 70 times higher than pristine CdS NPs.

2.2. Ternary Metal Sulfide Compounds

Bimetals sulfides display more outstanding HER performance during continuous catalysis due to their unique bimetals synergistic effect and adjustable potential. Zinc indium sulfide (ZnIn$_2$S$_4$), one of the emblematic AB$_2$S$_4$ ternary metal chalcogenides, is a layered structure n-type semiconductor with a direct band gap. ZnIn$_2$S$_4$ can exist in three different crystal polymorphs (cubic, trigonal, and hexagonal), with the hexagonal phase being the most thermodynamically stable structure.

Tao et al. employed the wet-chemical method for the preparation of ultrathin MIn$_2$S$_4$ (M = Zn, Cd, and Ni) nanoplates with a thickness of 2 nm, using as-grown β-In$_2$S$_3$ nanoplates as a template [67]. Further optimization showed that loading of Ni NPs as co-catalysts, the 3.0 wt% Ni/ZnIn$_2$S$_4$ photocatalysts exhibited the highest H_2 evolution rate of 19.9 mmol h^{-1} g^{-1}, which is six times larger than the ZnIn$_2$S$_4$ NPs. Recently, ZnIn$_2$S$_4$ monolayers with dual defects (Ag dopants and nanoholes) for improved HER were also reported [68]. While the undoped ZnIn$_2$S$_4$ could produce HER of 32.6 µmol h^{-1} g^{-1}, the Ag-ZnIn$_2$S$_4$ showed 56.6 µmol h^{-1} g^{-1}. Most importantly, the Ag-doped ZnIn$_2$S$_4$ could achieve 29.1 µmol h^{-1} g^{-1} O$_2$ evolution, which was not seen for the undoped ZnIn$_2$S$_4$. The proposed mechanism and the obtained reaction yield are given in Figure 9a.

In order to overcome the intrinsic limitations of the MoS$_2$, Lei et al. prepared a cobalt-modified amorphous molybdenum sulfide (Co-MoS$_x$) co-catalyst [69]. The optimized ZnCdS/Co-MoS$_x$ (Co/Mo = 1/4, 1 mol%) photocatalyst showed the highest HER rate of 551.48 µmol g^{-1} h^{-1} with an AQE of 21.7% at λ = 420 nm. The achieved rate was superior to that of ZnCdS/MoS$_x$ and pristine ZnCdS by 1.4 times and 23 times, respectively.

As stated above, the photocatalytic activity of NiS towards hydrogen generation is practically limited by the strong sulfur-hydrogen bonds. The weakening of this bond strength was achieved by introducing Cu atoms into the amorphous NiS$_x$ (a-NiS$_x$) co-catalyst, which led to the formation of the electron-rich active S sites [70]. The as-synthesized co-catalyst was anchored onto TiO$_2$ to form a-NiCuS$_x$/TiO$_2$ composite photocatalysts. The optimized CuS$_x$/TiO$_2$ (3:1) photocatalyst exhibited an improved H_2 evolution rate of 427.9 µmol g^{-1} h^{-1} with an AQE of 34.67% using methanol as a sacrificial reagent, which is superior compared to the a-NiS$_x$/TiO$_2$ with 226.1 µmol g^{-1} h^{-1}. Xu et al. reported a CuGaS$_2$ (CGS) photocatalyst synthesized by a one-step solid-phase sintering method [71]. It was shown that when the Cu to Ga atom ratio is 1: 1.4 in the raw material, the prepared CuGaS$_2$ exhibited the highest visible-light (λ > 420 nm) H_2 production rate reaching to 1.12 mmol g^{-1} h^{-1}. Moreover, loading with Ruthenium as a co-catalyst, the H_2 production rate of CuGaS$_2$@Ru was further promoted to 3.38 mmol g^{-1} h^{-1}. Wang et al. prepared CuInS$_2$ microflowers via the solvothermal method and decorated them with CdSe QDs on the surface. The prepared CdSe/CuInS$_2$ microflowers showed an improved photocatalytic H_2 production rate of 10,610.37 µmol g^{-1} h^{-1} with an AQE of 48.97% at 420 nm [72]. The enhanced photocatalytic H_2 evolution was related to the formation of a p-n heterostructure with improved light absorption ability, enhanced charge transfer efficiency, and a reduced recombination rate of the photogenerated electrons and holes. Also, the one-step alkaline hydrothermal strategy was used to prepare Ni-doped Mn$_{0.5}$Cd$_{0.5}$S with different Ni doping concentrations [73]. It was shown that 3% Ni-doped Mn$_{0.5}$Cd$_{0.5}$S could obtain the highest rate of 108.3 mmol g^{-1} h^{-1} at λ > 420 nm, which is nearly 14.4 times more than undoped counterpart (7.5 mmol g^{-1} h^{-1}). The proposed charge transfer mechanism, together with the obtained reaction yield, is shown in Figure 9b.
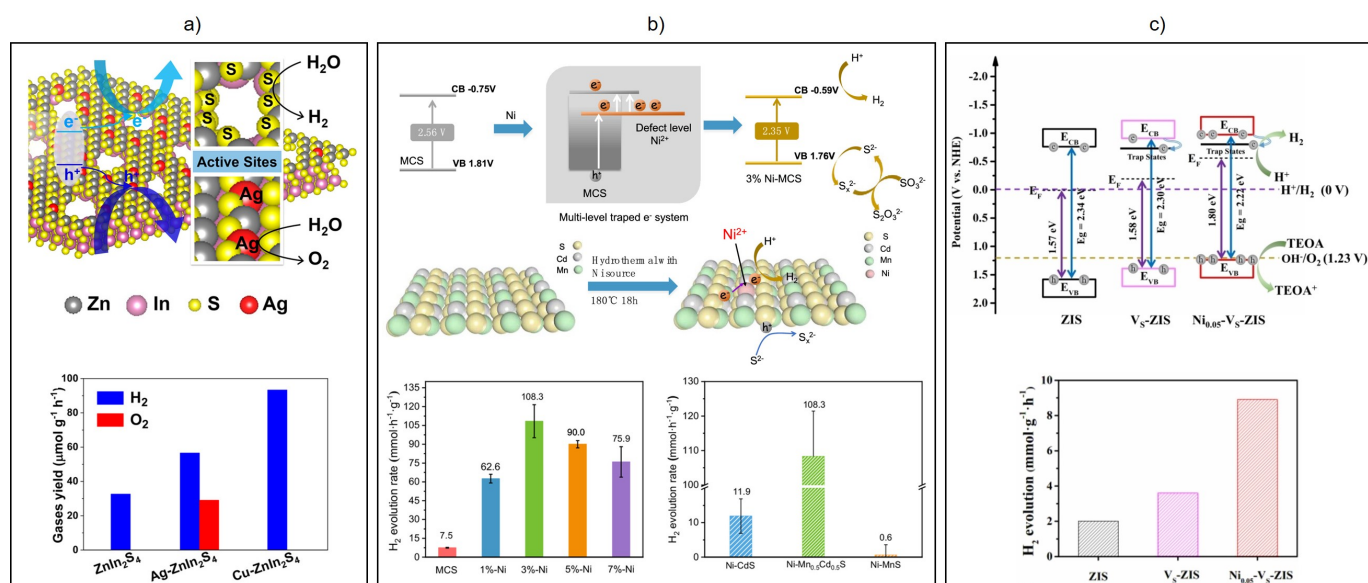
Figure 9. (**a**) Schematic illustration of the dual-defect (Ag dopants and nanoholes) configuration established on $ZnIn_2S_4$ monolayers and their role in promoting O_2 and H_2 evolution reactions during photocatalytic water splitting [68]. Copyright 2021, American Chemical Society. (**b**) Schematic illustration for the H_2 evolution mechanism for 3% Ni doped $Mn_{0.5}Cd_{0.5}S$ photocatalyst [73]. Copyright 2022, Wiley-VCH. (**c**) Schematic illustration of the band structure of ZIS, VS-ZIS and $Ni_{0.5}$-VS-ZIS [74]. Copyright 2021, Wiley-VCH. The corresponding HER yields for each optimized photocatalyst are given in the bottom panel.

Engineering sulfur vacancies supplemented by metal doping have been shown as a promising route to improve photocatalytic H_2 evolution. In this regard, ultrathin $ZnIn_2S_4$ nanosheets functionalized by sulfur vacancies and nickel dopants were reported [74]. It was shown that the S vacancies lower the CB minimum, enhance the photogenerated charge reduction capacity, and improve the lifetime of photoexcited states. Moreover, introducing Ni dopants shifts the Fermi level upward, leading to enhanced charge carrier separation and a reduced recombination rate. Thus, the synergistic effects lead to an 8.91 mmol g^{-1} h^{-1} H_2 evolution rate under Vis-light irradiation. The proposed charge transfer mechanism, together with the obtained reaction yield, is shown in Figure 9c. In order to improve photocatalytic hydrogen yield, the biomineralization method has also been recently employed. Thus, Zn-doped CdS ($Cd_{1-x}Zn_xS$) with various Zn^{2+}/Cd^{2+} ratios was synthesized by engineered *Escherichia coli* with a surface-displayed biomineralization system [75]. More specifically, bacterial-synthesized $Cd_{1-x}Zn_xS$ with an average particle size of <50 nm was deposited on the bacterial cell surface, which led to more material loading. The optimized $Cd_{1-x}Zn_xS$ with a 0.044 molar ratio of Zn/Cd showed an improved HER of 1.146 μmol h^{-1} g^{-1}.

As already given examples above, one of the main trends to improve photocatalytic H_2 production is a search for new architectures. For example, hollow $Cu_2MoS_4/ZnIn_2S_4$ heterostructural nanocubes with intimate-contact interface were reported as a self-template method [76]. The optimized 15 wt% $Cu_2MoS_4/ZnIn_2S_4$ sample exhibits the highest hydrogen production rate of 8103 μmol h^{-1} g^{-1}, which is four-fold improvement compared to the clean $ZnIn_2S_4$. The improved activity was ascribed to more active sites, increased light absorption by hollow nanocubes, and a built-in electric field, which facilitates photogenerated holes from $ZnIn_2S_4$ to Cu_2MoS_4 with enhanced charge separation. A sphere-like, structured $ZnIn_2S_4$-rGO-$CuInS_2$ ternary heterojunction catalyst for visible-active photocatalytic hydrogen evolution from water splitting was reported [77]. The obtained photocatalyst exhibited hydrogen generation of 2531 μmol/g after 5 h. Based on photocurrent density and photoluminescence measurements, it was discussed that rGO acts as an electron transfer medium by reducing excited charge recombination and facilitating electron transfer in the ternary

composite. Chong et al. reported on atomic-level charge steering for photocatalytic water splitting in P-doped ZnIn$_2$S$_4$ (ZIS) bilayer nanosheets via Density Functional Theory [78]. It was revealed that the replacement of the S3 atom by substitutional phosphorus gave rise to the most stable P-ZIS structure. Furthermore, P-ZIS was shown to have a lower band gap energy, an upshift of the valence band maximum (VBM), an increase in electron density at the VBM, and a lower H* adsorption-desorption barrier, which are essential parameters for H$_2$ evolution kinetics. Thus, the p-type doping strategy was shown as a promising route for improved H$_2$ evolution from water splitting.

2.3. Metal Sulfide and Metal Oxide Heterostructures

In order to design an efficient interface, Lin et al. produced a 2D/2D atomic double-layer WS$_2$/Nb$_2$O$_5$ shell/core photocatalyst (DLWS/Nb$_2$O$_5$) [79]. It was revealed that due to the unusual interface, the average lifetime of charge carriers for DLWS/Nb$_2$O$_5$ (180.97 ps) is remarkably reduced as compared to that of Nb$_2$O$_5$ (230.50 ps). Thus, the ultrafast charge transfer from Nb$_2$O$_5$ to atomic double-layer WS$_2$ was achieved, which gave rise to a high photocatalytic H$_2$ evolution rate of 237.6 µmol g^{-1} h^{-1}. Also, CoS/Nb$_2$O$_5$ heterojunctions were constructed by in-situ loading CoS co-catalyst on the surface of Nb$_2$O$_5$ nanosheets [80]. The femtosecond-resolved transient absorption spectroscopy revealed that the average lifetime of charge carriers for 10 wt% CoS/Nb$_2$O$_5$ (159.6 ps) is drastically shortened by contrast with that of Nb$_2$O$_5$ (5531.9 ps), thus similar to the DLWS/Nb$_2$O$_5$ rapid charge transfer from Nb$_2$O$_5$ to CoS could be achieved. The designed photocatalyst showed H$_2$ evolution rate of 355 µmol g^{-1} h^{-1}, which is up to 17.5 times higher than the pristine Nb$_2$O$_5$. By using the hydrothermal-physical mixture method, a Mo$_2$S$_3$/Bi$_2$O$_2$CO$_3$ composite with a unique n-n heterojunction and 2D structure was successfully prepared [81]. The optimized co-catalyst with the mass ratio of Mo/Bi-3% showed the highest H$_2$ evolution rate of ∼160 µmol.

Bismuth vanadate (BiVO$_4$) is another promising catalyst, which has been employed for solar-driven water splitting and H$_2$ production [82]. Recently, a step-scheme photocatalyst was developed by spatial deposition of MnO$_x$ and CdS NWs on a 3D decahedron BiVO$_4$ surface [83]. The synthesized CdS/MnO$_x$-BiVO$_4$ photocatalyst containing 5% of CdS demonstrated the highest H$_2$ and O$_2$ production rates of 1010 and 510 µmol g^{-1} h^{-1}, respectively, with an AQE of 11.3% without any sacrificial reagent. The existence of oxygen vacancies, effective charge separation and transport, and a significant interaction of co-catalysts (MnO$_x$ and Pt) with photocatalysts (BiVO$_4$ and CdS) in the CdS/MnO$_x$-BiVO$_4$ heterojunction were shown to be the major factors for boosted photocatalytic activity. It should be noted that especially for simultaneous O$_2$ generation, the single MS photocatalysts are not favorable because of the severe self-photooxidation or photocorrosion, which, however, can be altered by combining with other co-catalysts. In this regard, the development of MS-based Z-scheme photocatalyst, where the photogenerated holes in MS can be successfully carried away, is an effective approach (see Figure 6 for the Z-scheme photocatalysts) [84]. Heterostructure composite photocatalyst was synthesized by combining the Nb$_2$O$_5$-MoS$_2$ (NM) with CdS/graphene and CuS/graphene (NM-CdS/G, NM-CuS/G) via hydrothermal method [85]. While the NM photocatalyst showed a relatively low photocatalytic activity with a H$_2$ evolution rate of 1.6 mmol g^{-1} h^{-1}, the NM-CuS/graphene and NM-CdS/graphene composites showed remarkably enhanced H$_2$ evolution rates of 7.1 and 8.7 mmol g^{-1} h^{-1}, respectively. Thus, the combination of wide and narrow band gap semiconductors resulted in a fast charge separation process and a possibly improved lifetime of the charge carriers. Also, hierarchically porous hydrangea-like In$_2$S$_3$/In$_2$O$_3$ heterostructures were reported through a simple in situ oxidization process [86]. The new heterostructures exhibited superior photocatalytic activity (683.8 µmol/g) to the In$_2$S$_3$ and In$_2$O$_3$, that was assigned to enhanced interfacial charge transfer because of heterostructures and hierarchically porous heterostructures, which increases the number of active sites and improves the permeability. See Figure 10b for the proposed photocatalytic charge transfer mechanism and HER plot.

A Vis-light active hierarchical $Co_9S_8/ZnIn_2S_4$ photocatalyst was designed by decorating Co_9S_8 NPs onto the $ZnIn_2S_4$ nanoflower through a two-step solvothermal process and applied for photocatalytic H_2 evolution [87]. Due to sulfide-sulfide integrations in a hierarchical flower-like $Co_9S_8/ZnIn_2S_4$ photocatalytic heterojunction, large surface areas with rich active centers, effective separation and transfer of photoinduced electrons and holes were achieved. Correspondingly, the optimized $Co_9S_8/ZnIn_2S_4$ photocatalyst showed remarkably improved HER of 12.67 mmol h^{-1} g^{-1} with high stability, which is 6 times higher than that of single $ZnIn_2S_4$ photocatalyst under visible-light irradiation. The proposed photocatalytic charge transfer mechanism, together with the obtained yield, is shown in Figure 10b.
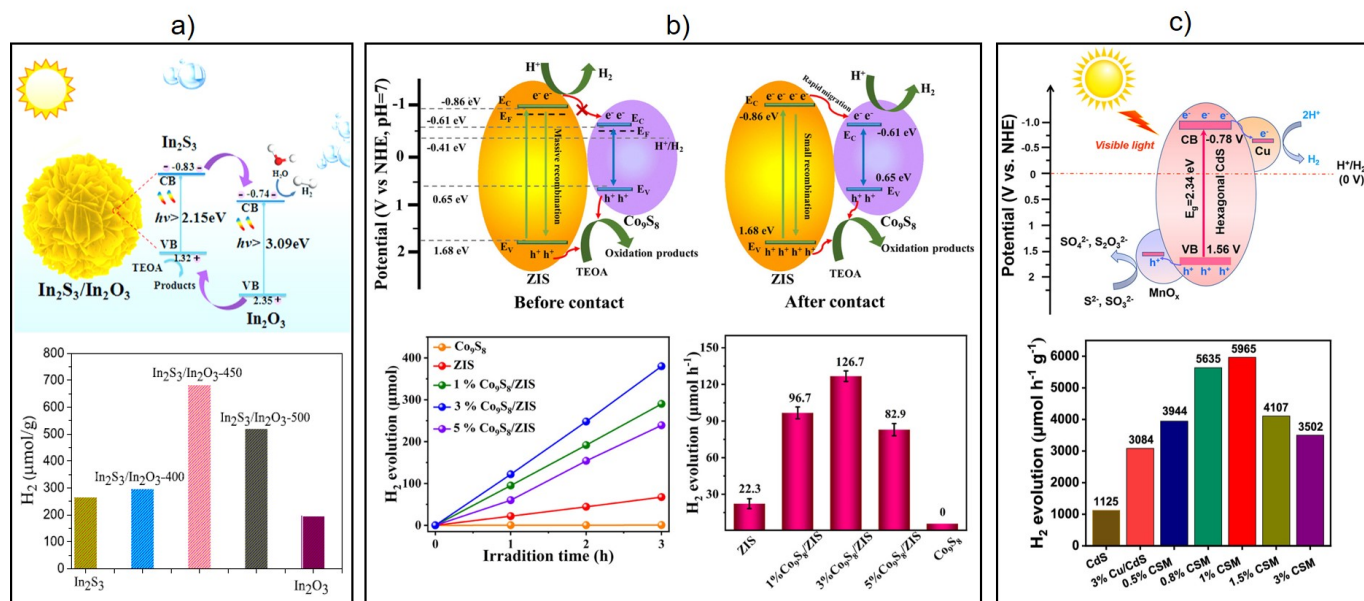
Figure 10. Schematic illustration of photocatalytic hydrogen evolution mechanism and corresponding HER plots for different metal sulfide and metal oxide heterostructures. (**a**) In_2S_3/In_2O_3 [86] Copyright 2022, Elsevier. (**b**) $Co_9S_8/ZnIn_2S_4$ [87] Copyright 2022, American Chemical Society. (**c**) $Cu/CdS/MnO_x$ [88] Copyright 2021, American Chemical Society.

Ta_2O_5 is another promising photocatalyst, which has been studied in the last years [89], also for the photocatalytic H_2 generation [90]. Recently, a $Cu_2S/Ta_2O_5/CdS$ ternary nanocomposite photocatalyst was fabricated by a solid-state approach and applied for photocatalytic hydrogen evolution [91]. It was shown that in the resulting structure, the Cu_2S, Ta_2O_5, and CdS form six-petals, nanorods, and random-spherical morphology, respectively. The optimized $Cu_2S/Ta_2O_5/CdS$ nanocomposite demonstrated a high rate of H_2 evolution of 131 mmol h^{-1} g^{-1} being remarkably higher than that of its constituents.

It is known that preparing photocatalysts deposited on semiconductors can effectively restrain charge recombination. In this regard, a $Cu/CdS/MnO_x$ (CSM) heterostructured photocatalyst with a spatial separation of the photoinduced charge carriers was reported [88]. It was shown that while a reduction co-catalyst Cu NPs tend to capture electrons, the oxidation co-catalyst, MnO_x NPs, collects the photogenerated holes. Time-resolved fluorescence spectra (TRPL) and photoelectrochemical characterization showed that the lifetime of photogenerated carriers improved, and surface-reactive HER kinetics were accelerated. As a result, the optimized 1% CSM photocatalyst showed a maximum HER of 5965.03 h^{-1} g^{-1} being ~5.3 higher than the single CdS photocatalyst. The proposed photocatalytic charge transfer mechanism, together with the obtained HER, is given in Figure 10c.

Step-scheme heterojunction composite photocatalyst based on $W_{18}O_{49}/Mn_{0.2}Cd_{0.8}S$ was produced via the physical stirring method and employed for photocatalytic hydrogen production under Vis-light illumination [44]. It was revealed that the H_2 evolution rate was

highest (5373 µmol h^{-1} g^{-1}) for the load ratio of W$_{18}$O$_{49}$ was 5%. Consequently, the formation of S-scheme heterojunction between W$_{18}$O$_{49}$ and Mn$_{0.2}$Cd$_{0.8}$S contact interface was shown as the reason for the improved H$_2$ production. Thus, the S-scheme heterojunction promotes the consumption of ineffective electrons and holes, improves the effective charge separation and transfer, and lowers the activation energy of the catalytic reaction system, leading to enhanced photocatalytic H$_2$ evolution. Also, MoS$_2$@MoO$_3$ step S-scheme heterojunction photocatalyst was prepared through in-situ partial sulfidation [92]. The heterostructure interface was engineered through the in-situ vulcanization strategy, which gradually corrodes from the outside to the inside of the nanostructures. Thus, introducing S-atoms can replace oxygen atoms to build a S-rich surface and generate molybdenum sulfide. Afterward, the amount of thioacetamide (S source) was adjusted to control vulcanization and optimize the experimental conditions. The synthesized heterostructure photocatalyst showed H$_2$ production rate of 12,416.8 µmol h^{-1} g^{-1}.

Metal Sulfide and TiO$_2$-Based Photocatalysts

TiO$_2$ is one of the most studied and applied photocatalysts for versatile purposes ranging from wastewater treatment and indoor air purification [93] to organic synthesis [94,95]. Moreover, metal sulfides/TiO$_2$ heterostructures with a porous architecture possess the capability to enhance the photocatalytic activity of TiO$_2$. First of all, the porous structure provides an abundance of carrier charge transfer routes and surface reaction sites. Moreover, the appropriate number of MS deposited on TiO$_2$ significantly improves the electrical conductivity and light absorption capabilities.

Lin et al. reported a sea-urchin-like ReS$_2$ nanosheet/TiO$_2$ NP heterojunctions with an unusual charge edge-collection effect leading to a significant acceleration of charge separation and transfer [96]. The designed photocatalysts yielded H$_2$ evolution rate of 3.71 mmol h^{-1} g^{-1} with an AQE of 16.09%, which is ~232 times higher than the commercial P25 TiO$_2$. Anatase phase TiO$_2$ QDs-sensitized Cu$_2$S (Cu$_2$S/TiO$_2$) nanocomposites with varying concentrations of TiO$_2$ QDs were synthesized via a facile two-stage hydrothermal-wet impregnation method [97]. The as-synthesized co-catalyst showed H$_2$ evolution rate of ~45.6 mmol h^{-1} g^{-1} under simulated solar irradiation, which is ~5 and 2.4-fold higher than that of the pristine TiO$_2$ and Cu$_2$S, respectively.

Chen et al. synthesized the CoS$_x$-rGO/TiO$_2$ composite photocatalyst by employing two steps: first, the rGO nanosheets hydrothermally loaded onto TiO$_2$ NPs, and then CoS$_x$ nanodots (0.5–2 nm) photodeposited on the rGO nanosheets [98]. The produced CoS$_x$-rGO/TiO$_2$ (10%) composite photocatalyst exhibited H$_2$ production efficiency of 256.97 µmol g^{-1} h^{-1}, being ~12 times higher than that of rGO/TiO$_2$ photocatalyst and ~2 times higher than that of CoS$_x$/TiO$_2$. It was proposed that rGO nanosheets facilitate the rapid transfer of photo-induced carriers from TiO$_2$ to CoS$_x$ nanodots and that CoS$_x$ nanodots thereafter function as active sites for H$_2$ production. In another study, the TiO$_2$@CuS double-shell nanoboxes were constructed via a multistep control strategy involving template participation [99]. The optimized TiO$_2$@CuS double-shell nanoboxes exhibited H$_2$ production rate of 2467 and 173 µmol g^{-1} h^{-1} under full-spectrum and near-IR irradiation, respectively.

Bismuth sulfide (Bi$_2$S$_3$) has also recently been considered as an effective co-catalyst (i.e., with TiO$_2$) because of its small band gap (1.28 eV), strong visible light absorption capacity (450–700 nm), and large negative conduction band (CB) potential. The amorphous BiS$_x$ nanodots with the size of 0.5–2 nm were loaded on TiO$_2$ surface to facilitate the photocatalytic H$_2$ generation [100]. The BiS$_x$/TiO$_2$ photocatalyst was synthesized by an Ethylenediaminetetraacetic acid (EDTA)-assisted two-step process, which included the adsorption of the Bi(III)-EDTA ions on TiO$_2$ and the in-situ formation of amorphous BiS$_x$ nanodots. The optimized BiS$_x$/TiO$_2$(1.0 wt%) photocatalyst showed the maximum photocatalytic H$_2$ production rate of 803.2 µmol h^{-1} g^{-1} with an AQE of 3.86%, which is 83.6 and 1.6 folds of the clean TiO$_2$ and crystalline Bi$_2$S$_3$-modified TiO$_2$ (c-Bi$_2$S$_3$/TiO$_2$), respectively. The enhanced photocatalytic H$_2$ production was assigned to the amorphous BiS$_x$ nanodots

providing more unsaturated active S atoms, which act as the efficient H_2 evolution active sites. Effective hydrogen evolution from water splitting under solar light irradiation was investigated using ZnS-PbS QDs loaded onto a Au/TiO_2 photocatalyst [101]. In the presence of 20 wt% methanol as a sacrificial reagent to photocatalyze for 5 h, 5011 µmol g^{-1} h^{-1} HER was observed. Nguyen et al. utilized polyvinyl alcohol (PVA) as a binder compound for combining MoS_2 and TiO_2 nanotube arrays (TNAs) to improve photoelectrochemical (PEC) water splitting ability [102]. They showed that by a thermal treatment process, the formation of the π-conjunction in the PVA structure enhanced the PEC performance of MoS_2/TNAs, exhibiting linear sweeps in the anodic direction with the current density over 65 µA/cm^2 at zero bias voltage vs. Ag/AgCl.

In general, ternary-metal-sulfide/TiO_2 photocatalysts are expected to have lower toxicity, a tunable band structure, and favorable chemical stability, enabling a higher HER over the binary-metal-sulfide/TiO_2. In this regard, $NiWS_x$ nanodot-modified TiO_2 ($NiWS_x$-ND/TiO_2) photocatalysts were prepared by evenly anchoring ultrasmall amorphous $NiWS_x$ nanodots (~2 nm) onto TiO_2 surface by means of a facile photodeposition strategy [103]. The optimized $NiWS_x$-ND/TiO_2 (3 wt%) photocatalyst manifested the maximum H_2 generation efficiency of 4580 µmol h^{-1} g^{-1} with the corresponding AQE of 13%. Dai et al. reported a S-scheme heterojunction photocatalyst by coupling the $ZnCo_2S_4$ NPs on the surface of TiO_2 through simple solvothermal method [104]. The prepared nanocomposite photocatalyst exhibited H_2 evolution efficiency of 5580 µmol h^{-1} g^{-1} with an AQE of 11.5% at 420 nm, which is 88.3 times and 54.3 times that of TiO_2 and $ZnCo_2S_4$ NPs, respectively. It was discussed that the S-scheme electron transfer path facilitates better electron-hole separation alongside improved charge transfer efficiency. While the $ZnCo_2S_4$ NPs significantly enhance the visible light absorption, leading to a high H_2 yield. The resulting efficiency and proposed photocatalytic mechanism are summarized in Figure 11.
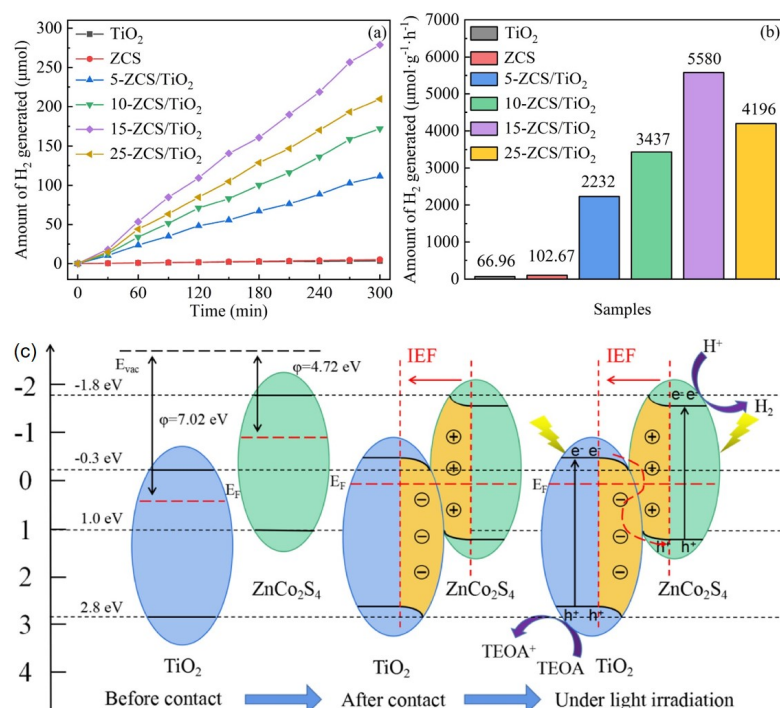
Figure 11. Time evolution (**a**) and average rate (**b**) of photocatalytic hydrogen production activity over the TiO_2, $ZnCo_2S_4$ (ZCS), 5-ZCS/TiO_2, 10-ZCS/TiO_2, 15-ZCS/TiO_2 and 25-ZCS/TiO_2 photocatalysts. 5, 10, 15, and 25 are the mass proportion of ZCS in the composite. (**c**) Schematic illustration of the photocatalytic mechanism over the 15-ZCS/TiO_2 photocatalyst: Thus, under Vis-light irradiation, the internal electric field (IEF) induces charge transfer (**a**), separation, and the formation of S-scheme heterojunction (**b**) to realize photocatalytic hydrogen evolution (**c**) [104]. Copyright 2022, Elsevier.

Also, a TiO_2 nanoplate/amorphous MoS_2 QD (a-MoS_2) composite was prepared via in situ sulfuration of MoO_2/TiO_2 [105]. It was shown that in this composite, the intimate chemical bonding instead of electrostatic adsorption between TiO_2 and MoO_2 enables effective electron transfer from TiO_2 to a-MoS_2. The optimized a-MoS_2/TiO_2 nanocomposite exhibited a maximum H_2 yield of 880.3 $\mu mol\ h^{-1}\ g^{-1}$. In another study, ultrathin TiO_2 nanosheets were integrated into the growth of $ZnIn_2S_4$ to produce TiO_2-$ZnIn_2S_4$ heterostructure nanoflowers in order to design a direct Z-scheme heterojunction photocatalyst with an improved PHE [106]. It was revealed that the formed direct Z-scheme heterojunction can consume residual photogenerated holes of $ZnIn_2S_4$ and enable water oxidation to occur solely at the TiO_2 site, improving the overall stability of the system. The optimized DZH nanoflowers showed enhanced photocatalytic water splitting activity of 214.9 $\mu mol\ h^{-1}\ g^{-1}$ for H_2 evolution and 81.7 $\mu mol\ h^{-1}\ g^{-1}$ for O_2 evolution.

2.4. Metal Sulfide/g-C_3N_4 Heterostructures

Combining suitable co-catalysts and simultaneous interface engineering is another promising strategy for photocatalytic HER enhancement. In this regard, Wang et al. reported a CN/A-MoS_2/Pt photocatalyst using amorphous MoS_2 (a-MoS_2) as the conformal multifunctional intermediate layer between g-C_3N_4 and Pt [107]. They showed that a conformal chemically bonded interface and low overpotential for the H_2 evolution reaction lead to enhanced interface charge transfer and photochemical reaction kinetics. Thus, under Vis-light illumination, 5830 $\mu mol\ h^{-1}\ g^{-1}$ HER was achieved, which is more than an 83-fold enhancement compared with the g-C_3N_4. The detailed parameterization and corresponding HERs, together with the proposed photocatalytic reaction mechanism, are given in Figure 12.
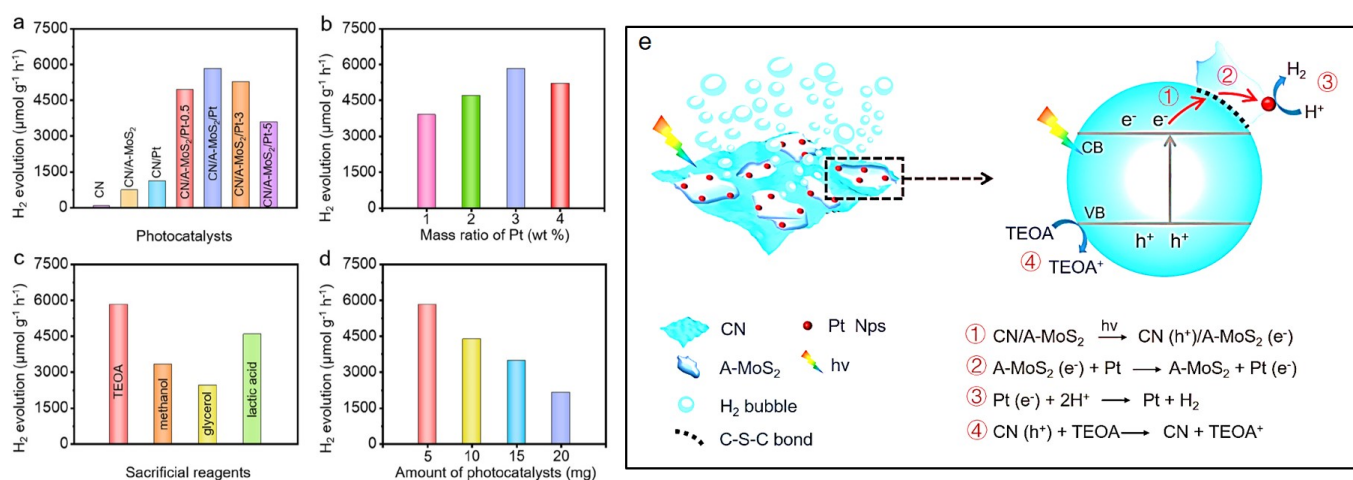
Figure 12. (**a**) Photocatalytic hydrogen production rate of various photocatalysts. (**b**) photocatalytic rate of CN/A-MoS_2/Pt with different mass ratios of Pt. (**c**) photocatalytic rate of CN/A-MoS_2/Pt measured in different sacrificial reagents. (**d**) photocatalytic rate of CN/A-MoS_2/Pt tested with different masses of the photocatalyst. (**e**) Proposed charge transfer mechanism for the CN/A-MoS_2/Pt photocatalysts [107]. Copyright 2021, American Chemical Society.

It should be noted that the effective surface area of the co-catalysts has a significant impact on photocatalytic performance. In this regard, it has been reported that g-C_3N_4 structures with a large surface area can be produced using a rapid high-temperature hydrothermal post treatment strategy with fast heat transfer and short processing time. Thus, the extended surface area resulted in about 5.1 higher HER compared to pristine g-C_3N_4 under Vis-light ($\lambda > 400$ nm) irradiation [108]. A ternary composite catalyst of MoS_2/Fe_2O_3/g-C_3N_4 via hydrothermal method was reported [109]. The fabricated composite photocatalyst demonstrated H_2 generation rate of 7.82 $mmol\ g^{-1}\ h^{-1}$, which is almost 5 times higher than the single-component g-C_3N_4 photocatalyst (1.56 $mmol\ g^{-1}\ h^{-1}$). The improvement

of its photocatalytic activity can be mainly attributed to its enhanced visible light absorption and the increased specific surface area. According to the earlier DFT investigations, in the MoS_2/g-C_3N_4 composite, the CB minimum and VB maximum of the g-C_3N_4 monolayer are roughly 0.83 eV, and 0.15 eV higher than those of the MoS_2 sheet [110]. As a result of the formed type-II band alignment, photoexcited electrons can easily migrate from the g-C_3N_4 monolayer to the MoS_2 sheet, resulting in a high hydrogen evolution reaction activity. Additionally, the charge transfer between MoS_2 and g-C_3N_4 generates a polarized field at the boundary, enabling effective separation of photogenerated carriers. A transition metal sulfide (Co_3S_4) produced from MOF was used to build an ohmic contacting Co_3S_4-CN heterojunction interface for enhanced photocatalytic H_2 generation [111]. It was revealed that electron injection from the lower work function Co_3S_4 to g-CN causes a significant interfacial electric field resulting in downward band bending in a g-CN semiconductor. Furthermore, the Co_3S_4-CN heterojunction facilitates exciton dissociation while removing a possible barrier for electron extraction from g-CN, facilitating charge carrier separation synergistically. The obtained co-catalyst showed H_2 evolution of $\sim$217.0 µmol g^{-1} h^{-1} upon visible light illumination. Chen et al. employed a light-induced deposition approach to precisely load NiS nanodots onto the surface of g-C_3N_4 to produce a bifunctional photocatalyst [42]. The obtained photocatalyst showed an enhanced photocatalytic H_2 evolution reaction and photocatalytic oxygen reduction. Particularly, the NiS@g-C_3N_4-30 displayed a H_2 evolution rate of 3297 µmol g^{-1} h^{-1} under visible-light illumination. It was discussed that the close interaction of the loaded NiS nanodots with the electron transfer sites of g-C_3N_4 nanosheets provides effective separation of photogenerated charge carriers and further accelerates the chemical reaction on the surface of the photocatalyst.

Considering that loading more NiS co-catalyst to function as active sites of g-C_3N_4 for improved photocatalytic H_2 generation, a facile sulfur-mediated photodeposition approach was developed [112]. It was shown that photogenerated electrons excited by Vis light reduce the S molecules absorbed on g-C_3N_4 surface to S^{2-}, and subsequently, a NiS co-catalyst is formed in situ on the g-C_3N_4 surface by a combination of Ni^{2+} and S^{2-}. The resulting NiS/g-C_3N_4 photocatalyst exhibited H_2 generation rate of 244 µmol g^{-1} h^{-1}.

The PtS/g-C_3N_4 co-catalyst was produced by loading 2D PtS nanorectangles with a length of $\sim$7 nm and width of $\sim$5 nm on the surface of g-C_3N_4 nanosheets utilizing in situ vapor-phase growth [113]. The constructed compound showed an unusual metal sulfide-support interaction, which promoted stabilization of the geometrical structure and energy-band structure, leading to acceleration of charge transfer, and reduction of hydrogen adsorption free energy of PtS/CN. The characteristics mentioned above gave rise to a high H_2 generation rate of 1072.6 µmol g^{-1} h^{-1} with an AQE of 45.7% at 420 nm. This is $\sim$13.3 and $\sim$1532.3 times enhancement in comparison with the Pt NPs/g-C_3N_4 nanosheets and pristine g-C_3N_4 nanosheets, respectively. In another study, ultrasmall fine Pt NPs and MoS_2 nanosheets were deposited on the surface of g-C_3N_4 as co-catalyst [114]. While MoS_2 could efficiently induce structural reconstruction of g-C_3N_4, resulting in surface charge redistribution, the boosted electrons localized in the S and N atoms were conducive to the reduction of Pt^{4+} via strong metal-support contact, hence enhancing charge separation and transfer. Consequently, the synthesized Pt/MoS_2/g-C_3N_4 composite exhibited a high photocatalytic hydrogen production rate up to 1595.3 µmol g^{-1} h^{-1} with an AQE of 30.9% at 435 nm, which is 87.6 times higher than that of the clean g-C_3N_4.

Wei et al. synthesized ternary ZnS-NiS_2/g-C_3N_4 and NiS_2-ZnS/g-C_3N_4 composites by a thermal polymerization and post-co-deposition-sulfidation methods to promote visible light absorption as well as charge separation and transfer [115]. The as-synthesized NiS_2-ZnS/CN(0.4) and ZnS-NiS_2/CN(0.4) photocatalysts showed PEH rate of 283.3 and 302.7 µmol h^{-1} g^{-1}, respectively. The 2D SnS/g-C_3N_4 nanosheets prepared by a facile ultrasonic and microwave heating method were also reported for enhanced H_2 evolution [116]. Furthermore, after being loaded with MoO_3 particles, the photocatalyst stability improved significantly due to the produced Z-scheme heterojunction. As a result, the enhanced light-harvesting capability of the composite, reduced charge-transfer resistance, improved

electrical conductivity, and the co-catalyst effect of SnS facilitated a higher H_2 generation rate of 818.93 µmol h^{-1} g^{-1} under AM1.5G irradiation. Also, g-CN/MoS$_2$ composite was synthesized via an in-situ gas-solid reaction where rodlike MoO$_3$ was sulfurized to form MoS$_2$ by the byproduct generated during the thermal condensation of thiourea [117]. The H_2 evolution rate improved from 0.99 to 13.31 µmol h^{-1} g^{-1}, which is 13.44 times higher than that of clean g-CN. Similarly, 1T/2H hybrid WS$_2$ was prepared as a non-noble metal co-catalyst for g-C$_3$N$_4$ using a straightforward synthesis technique based on an in situ gas-solid phase reaction [118]. Because of the hybrid crystal phase and the presence of S defects in WS$_2$, the photocatalytic hydrogen evolution efficiency of the co-catalyst improved noticeably, increasing from 0.32 to 34.76 µmol g^{-1} h^{-1}. In another study, red-phosphor-doped Co$_9$S$_8$ (P-Co$_9$S$_8$) was synthesized by a hydrothermal process [119]. It was revealed that the introduction of P-Co$_9$S$_8$ improved the electrical conductivity and surface area of the composite along with reducing the over-potential of H_2 evolution. Consequently, the optimized 25% P-Co$_9$S$_8$/g-C$_3$N$_4$ exhibited H_2 evolution rate of 4362 µmol h^{-1} g^{-1} under UV and visible light, which is roughly 121.2 times improved in comparison with the pristine g-C$_3$N$_4$. According to the photoelectrochemical analysis, the designed photocatalyst was assigned as a Type-I system, where more electrons on the CB of P-Co$_9$S$_8$ to participate in the H_2 evolution processes.

In parallel to the binary metal sulfides, ternary metal sulfides were also employed to produce co-catalyst together with g-C$_3$N$_4$ for photocatalytic H_2 generation. In this regard, in order to improve the photocatalytic water splitting reactivity of g-C$_3$N$_4$, ternary ZnCo$_2$S$_4$ was coated on its surface [120]. The optimized 25 wt%-ZnCo$_2$S$_4$/g-C$_3$N$_4$ showed H_2 evolution rate of 6619 µmol h^{-1} g^{-1}, which is 55.2 times higher than that of g-C$_3$N$_4$ alone. Thus, the enhanced H_2 production activity was assigned to the presence of both zinc and cobalt ions in ZnCo$_2$S$_4$, which reduced the H_2 evolution overpotential and charge recombination rate. The obtained photocatalytic process was ascribed as an S-scheme charge transfer route based on trapping experiments for active species. Also, copper-nickel sulfide was anchored on the g-C$_3$N$_4$ for increasing the photocatalytic H_2 evolution [121]. It was revealed that copper-nickel sulfides can effectively suppress deep trapping states of active charge in g-C$_3$N$_4$ improving the efficiency of the shallow trapped electron transfer through a single C-S bond for enhancing Vis-light-driven photocatalytic H_2 production. The synthesized co-catalyst showed H_2 evolution rate up to 752.8 µmol h^{-1} g^{-1} being 470 times higher than that of clean g-C$_3$N$_4$ [121]. Employing femtosecond time-resolved spectroscopy, it was also shown that the strong interaction between copper-nickel sulfide and g-C$_3$N$_4$ favored the hole transfer from copper-nickel sulfide to the trap state of g-C$_3$N$_4$ leading to a remarkable near-IR-driven photocatalytic H_2 production (0.32 µmol h^{-1} g^{-1}, $\lambda > 800$ nm).

2.5. Metal Sulfide/MOFs (COFs) Heterojunction Photocatalysts

One of the viable techniques for solar energy-driven water splitting is the development of metal-organic frameworks and covalent-organic framework (COF)-based heterostructure. Wang et al. fabricated a direct Z-scheme heterostructure COF-metal sulfide hybrid (T-COF@CdS) with shell-core architecture by self-polymerization of 1,3,5-benzenetricarboxaldehyde and 2,4,6-tris(4-aminophenyl)-1,3,5-triazine in situ on CdS NPs [122]. In these shell-core structures, the C-S chemical bonding generated between T-COF and CdS results in a tight and stable interface. Moreover, the T-COF shell acts as an oxidation site to avoid the photocorrosion of CdS and protects the catalytic centers of CdS against deactivation, leading to long-term stability. Thus, the fabricated Z-scheme T-COF@CdS-3 heterostructure exhibited a high AQE of 37.8% at $\lambda = 365$ nm.

MOFs have been widely applied in photocatalytic hydrogen production because of their high surface area, semiconductor-like behavior, and great active sites. For example, Mn$_{0.2}$Cd$_{0.8}$S NRs assembled on the surface of Ni-MOF-74 with flake morphology, where the Ni-S bonds between Ni-MOF-74 and Mn$_{0.2}$Cd$_{0.8}$S form a unique transfer channel for photo-induced charge carriers [123]. Thus, the potential energy difference between the two

compounds enables fast injection of the photogenerated electrons in the CB of $Mn_{0.2}Cd_{0.8}S$ into the CB of Ni-MOF-74, which remarkably inhibits the electron-hole recombination. Thus the improved carrier lifetime, fast charge transfer rate, and lower overpotential lead to a high H_2 production rate reaching 7.104 mmol g^{-1} h^{-1}, which is 6.96 times that of $Mn_{0.2}Cd_{0.8}S$. A CdS@NiS photocatalyst using bimetallic MOFs as the precursor was also reported [124]. It was demonstrated that bimetallic Cd/Ni-MOFs can result in well-contacted heterogeneous interfaces between CdS and NiS, effectively facilitating photogenerated carrier separation and enhancing electron interface transport. The designed CdS@NiS photocatalysts showed a high photocatalytic HER of 42.7 mmol g^{-1} h^{-1}, and the corresponding AQE reaches 13.23% at 450 nm.

In another study, the microwave irradiation method was utilized to create the UIO-66(Ce)/ZnCdS composite using Ce-based MOF components [UIO-66(Ce)] [125]. It was revealed that ZnCdS NPs were decorated on the surface of UIO-66(Ce) and that UIO-66(Ce) considerably increased the H_2 generation ability of ZnCdS NPs by effectively enhancing the charge carrier separation. Thus, the UIO-66(Ce)/ZnCdS nanocomposite photocatalysts showed H_2 production rate of 3.958 mmol g^{-1} h^{-1}, which is roughly 1.95 times higher than that of ZnCdS (2.031 mmol g^{-1} h^{-1}).

Also, as an efficient $ZnIn_2S_4$-MOFL photocatalysts for robust photocatalytic hydrogen evolution, hollow tubular $ZnIn_2S_4$ modified by MOF-layers with In-MOF as precursor was demonstrated [126]. The DFT studies proved the decreased density of states (DOS) of $ZnIn_2S_4$ after coupling with the organic ligands. The established direct Z-scheme photocatalytic system synergistically promoted the separation of electron and hole pairs leading to high photocatalytic H_2 evolution. The H_2 evolution using this photocatalyst reached 28.2 mmol g^{-1} h^{-1}, which is roughly 14.8 times higher than that of pristine $ZnIn_2S_4$. Moreover, the photocatalyst showed AQEs of 22.67% at monochromatic light (350 nm) and the stable H_2 generation capability (5.7 mmol g^{-1} h^{-1}) under natural sunlight irradiation. Aiming for efficient electron-hole separation and carrier utilization in photocatalytic H_2 generation, Lian et al. employed MOF (NH_2-UiO-66) modified with inner Pt NPs and outer CdS NPs [127]. The designed ternary composite $Pt@NH_2$-UiO-66/CdS possessing a spatially separated, the hierarchical structure was employed for visible-light-driven H_2 evolution, which exhibited higher H_2 yields with an AQE of 40.3% at λ = 400 nm irradiation. The proposed photocatalytic mechanism and H_2 evolution rate are given in Figure 13a.
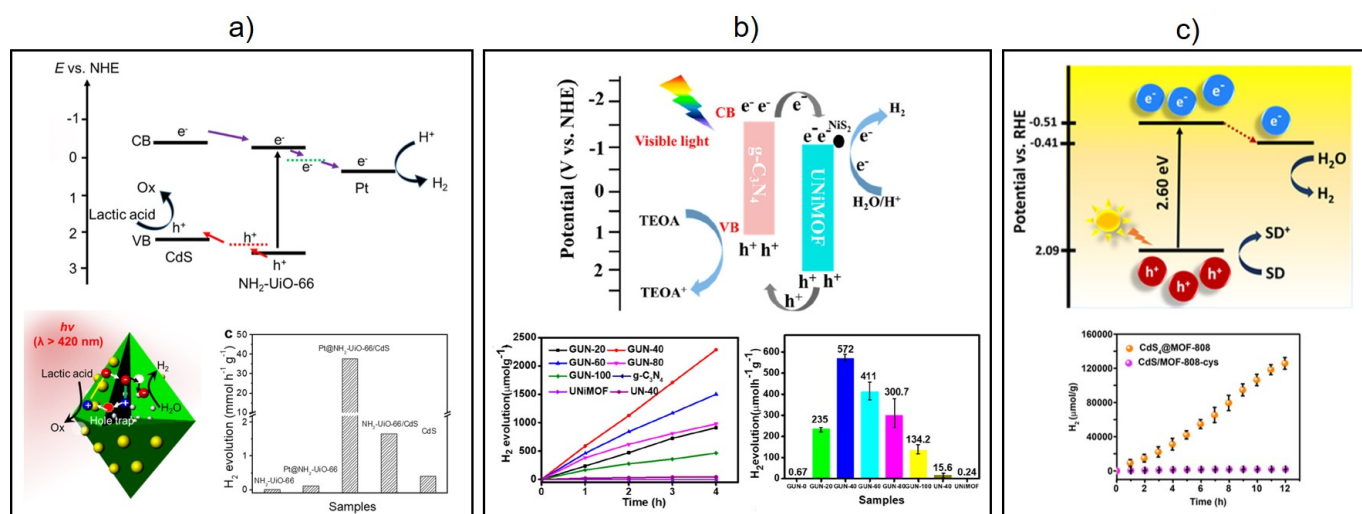
Figure 13. Proposed reaction mechanisms for the photocatalytic H_2 evolution and obtained H_2 production rates over different MS-based heterojunction photocatalysts. (**a**) $ZnIn_2S_4@CoS_2$ [127] Copyright © 2022 Springer Nature. (**b**) g-C_3N_4/UNiMOF/NiS_2 (GUN) [128] Copyright 2022, American Chemical Society. (**c**) CdS@MOF-808 [129] Copyright © 2022, American Chemical Society.

As we already discussed through this overview, stabilizing photoexcited states by suppressing charge recombination is one of the most important parameters for being good photocatalysts. In this regard, using two-dimensional (2D) UNiMOF as a precursor and by applying the partial hydrothermal sulfidation method, a g-C_3N_4/UNiMOF/NiS_2 (GUN) ternary heterojunction (TH) photocatalyst was synthesized [128]. As expected, the optimized GUN-40 heterojunction containing 40 mg of UNiMOF (GUN-40) exhibited enhanced HER of 572 µmol g^{-1} h^{-1} with a longer exciton recombination lifetime of $\tau = 12.12$ ns. This is remarkably higher than that of the pristine g-C_3N_4 (0.67 µmol g^{-1} h^{-1}, $\tau = 7.87$ ns) under Vis-light illumination. Also, the optimized GUN-40 photocatalyst showed an improved AQE up to 1.54 % at $\lambda = 450$ nm. Thus, the GUN TH structure significantly accelerates electron transport to the NiS_2 active site, improving the excited state lifetime, and minimizes the charge recombination rate, thus enhancing photocatalytic performance. The proposed photocatalytic mechanism and H_2 evolution rate are given in Figure 13b. Similarly, a CdS@MOF-808 composite photocatalyst where CdS NPs are confined inside the nanosized pores of Zr^{4+}-based MOF-808 was recently proposed [129]. It was shown that the confinement of the CdS NPs inside the MOF pores, close to the Zr^{4+} cluster, forms a shorter electron transfer route from CdS to the catalytic Zr^{4+} cluster. Thus, with an optimized load of 3.56 wt% CdS HER of 10.41 mmol g^{-1} h^{-1} from the water splitting was achieved. The proposed photocatalytic mechanism and HER are shown in Figure 13c. Moreover, a similar composite containing CdS NPs on the external surface, instead of cavities of MOF-808, showed a lower photocatalytic HER of 0.15 mmol g^{-1} h^{-1}.

Among other MOFs, zeolitic imidazolate frameworks (ZIFs), which are topologically isomorphic with zeolite, possess exposed metal sites, accessible carbon/nitrogen ligands, and good chemical stability, are attractive for solar-driven hydrogen generation. Recently, ZIF-67/CdS hollow sphere (HS) and ZIF-8/CdS HS heterostructures were synthesized through an in-situ self-assembly process, where the ZIF-67 and ZIF-8 are closely coated on CdS HSs to form "double-shell"-like structures with porous outer layers [130]. The optimal proportion of ZIF-67/CdS HS showed a HER of 1721 µmol g^{-1} h^{-1} under Vis-light illumination, which was ∼3 times higher than that of ZIF-8/CdS HS (555 µmol g^{-1} h^{-1}). The photocatalytic mechanism for the ZIF-8/CdS HS and ZIF-67/CdS HS was assigned as type-II and Z-scheme mechanisms, respectively. The synthetic route to composite formation alongside the morphological characterization, corresponding model structure and photocatalytic mechanism for the optimized ZIF-67/CdS HS are summarized in Figure 14. In this line, lollipop-shaped Co_9S_8/CdS nanocomposite via direct annealing of zeolitic imidazolate framework-67 (ZIF-67) as a template and CdS as a sulfur source was reported [131]. It was mentioned that the close proximity of these two materials facilitates electron transport and increases the number of active sites toward the desirable redox reaction. The as-prepared Co_9S_8/CdS resulted in a remarkably improved HER of 1852 µmol g^{-1} h^{-1} under Vis-light illumination. In another study, the ZIF-67 derived Co_3O_4 was used as precursor to prepare $ZnIn_2S_4$@CoS_2 photocatalyst [132]. The optimized structure possessing 5% CoS_2 showed the highest HER performance of 2768 µmol g^{-1} h^{-1} under the irradiation of simulated sunlight, which is three times higher than the $ZnIn_2S_4$ (879 µmol g^{-1} h^{-1}).
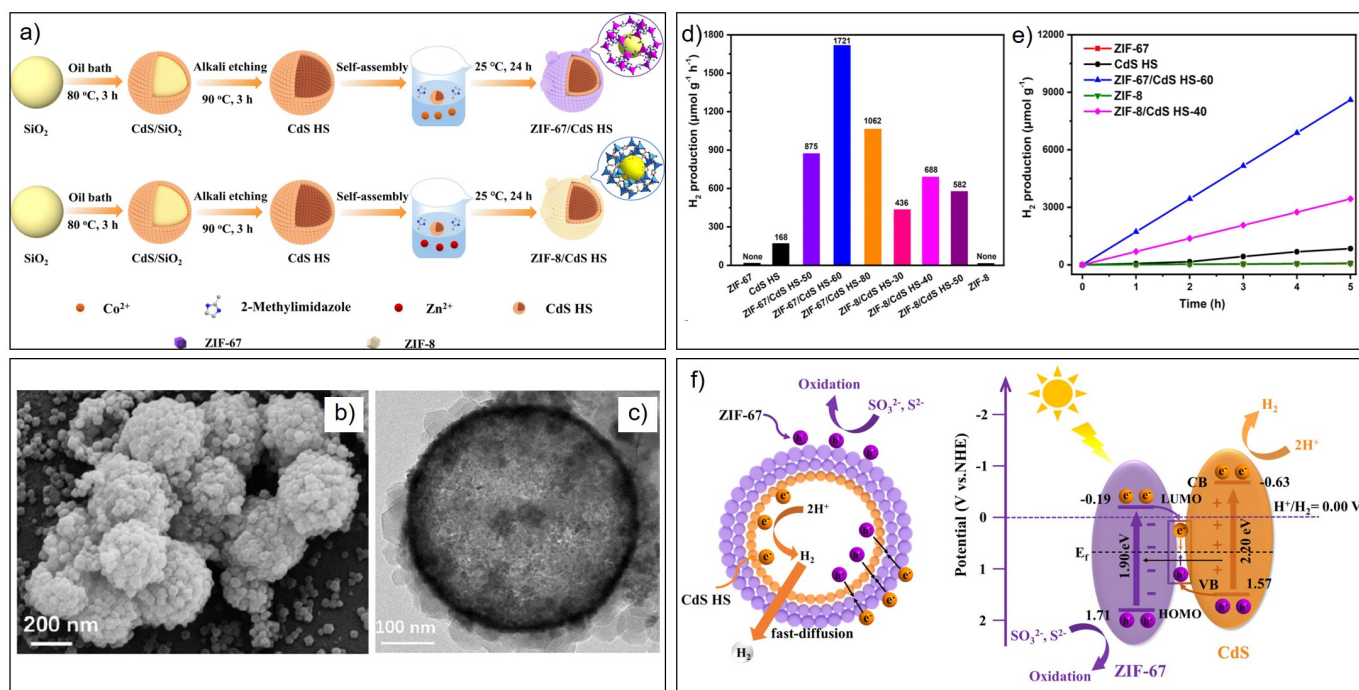
Figure 14. (**a**) The synthesis procedure of the ZIF-67/CdS HS and ZIF-8/CdS HS. (**b**) TEM and (**c**) SEM images of the ZIF-8/CdS HS heterostructures. CdS HSs are rapped with the ZIF-8 to form "double-shell" like structure, indicating close contact between the two components. (**d**) Hydrogen evolution rates and (**e**) time-dependent photocatalytic performances of various catalysts. (**f**) Schematic view of the charge transfer mechanism over the ZIF-67/CdS HS photocatalyst under Vis-light illumination [130]. Copyright 2022, American Chemical Society.

2.6. Hierarchical Metal Sulfide Photocatalysts

Hierarchical nano- and mesostructures are potential systems for catalysis, electrocatalysis, solar cells, membranes, and photocatalysis, among other applications. Regarding photocatalytic applications the layered (e.g., 2D) and multidimensional (e.g., 1D/2D, 1D/3D, etc.) hybrid heterostructures are particularly appealing. In addition to dimensional advantages (tunable band gap, large surface and interaction area, etc.), these structures enable formation of high energy facets and easy morphological modification, such as the design of membranes [133] and photonic crystals [57], which may enable further photocatalytic enhancement. Recently promising results have been achieved in this field. For example, an ultrathin 2D/2D $MoS_2/ZnIn_2S_4$ co-catalyst was designed and prepared employing two steps of the in situ hydro/solvothermal method [134]. It was suggested that the reduced dimensionality of the components enables the fast charge transfer and suppression of the photogenerated charge carriers recombination. 4 wt% ut-$MoS_2/ZnIn_2S_4$ exhibited the highest H_2 evolution rate of 221.71 µmol $g^{-1} h^{-1}$ under Vis-light irradiation ($\lambda > 420$ nm) with a corresponding AQE of 1.8%.

Another trend of the strategies toward photocatalytic enhancement is the improvement of sulfur vacancies (SV) in metal sulfide compounds. In this regard, CuS NPs, which possess suitable band gap energy [135,136], were employed to prepare CdS@CuS core-shell heterostructure photocatalyst by hydrothermal treatment and subsequent cation-exchange reactions [137]. The CdS-sulfur vacancies enriched by CuS via photoinduced interfacial charge transfer. The developed CdS-SV@CuS(5%) catalyst showed a significantly higher H_2 production rate of 1654.53 µmol $g^{-1} h^{-1}$. Similarly, 0D/2D NiS/CdS nanocomposite heterojunction photocatalyst with enhanced photocatalytic HER was reported [138]. There, the composite containing 25% molar ratio of NiS showed the highest HER at about 18.1 mmol $g^{-1} h^{-1}$. A Co_9S_8@$CdIn_2S_4$ heterostructure with hierarchical hollow construction and closely connected heterogeneous shells was also reported for photocatalytic H_2

evolution under visible light [47]. It was demonstrated that such a unique architecture may efficiently separate and transmit photoinduced charges while also providing a large surface area and exposing rich sites for photocatalytic redox processes. The designed photocatalyst showed HER of 4604 μmol h^{-1} g^{-1} under 1.5 AM simulated light irradiation. In other study, CoS$_x$/twinned-Cd$_{0.5}$Zn$_{0.5}$S (CoS$_x$/T-CZS) photocatalyst was produced through an in-situ deposition method [139]. Particularly, the formation of the zinc-blende/wurtzite (ZB/WZ) homojunction in T-CZS, as well as the heterojunction between CoS$_x$ and T-CZS promoted the charge separation in the bulk and surface of T-CZS. Consequently, T-CZS exhibited much higher activity compared to the zinc blende Cd$_{0.5}$Zn$_{0.5}$S (ZB-CZS) and wurtzite Cd$_{0.5}$Zn$_{0.5}$S (WZ-CZS) with single-phase. Introduction of amorphous CoS$_x$ improved H$_2$ evolution rate of 4 wt% CoS$_x$/T-CZS to 76.2 mmol g^{-1} h^{-1}. Recently, various hollow CoS-supported CdS catalyst (H-CoS/CdS) prepared by loading CdS onto the surface of H-CoS was also reported for H$_2$ production in pure water and simulated seawater [140]. The H$_2$ production rate of the as-synthesized co-catalyst from simulated seawater reached to 572.4 μmol g^{-1} h^{-1}. Thus, incorporating the h-CoS co-catalyst extended the light absorption range of CdS, improved the chemical stability, and significantly enhanced the charge separation leading to high photocatalytic efficiency. In another study, cobalt sulfide was employed to produce 1D-2D CdIn$_2$S$_4$/carbon nanofibers (CNFs)/Co$_4$S$_3$ tandem Schottky heterojunction via in-situ electrospinning combined with a hydrothermal method [141]. The optimised composite showed the H$_2$ production activity rate of 25.87 mmol g^{-1} h^{-1} with an AQE of 19.56% at λ = 365 nm. Similarly, in order to mitigate the recombination of electrons and holes, MoS$_2$ nanosheets with rich active sites were modified on the surface of CdS NRs by a room-temperature sonication treatment [142]. The obtained 6% MoS$_2$/CdS nanocomposites co-catalyst showed improved H$_2$ evolution rates of 63.71 and 71.24 mmol g^{-1} h^{-1} in visible light and simulated solar light irradiation, respectively. The AQE of the 6% MoS$_2$/CdS nanocomposite at 420 nm reached 33.62%. The enhanced photocatalytic activity was assigned to the extra photogenerated charge carriers, which enhanced the charge separation and transfer ability of the MoS$_2$/CdS co-catalyst. By in-situ epitaxially growing 2D ZnIn$_2$S$_4$ nanosheets onto the surface of 1D faulty CdS NRs, atomic CdS/ZnIn$_2$S$_4$ heterojunctions were produced [143]. The optimized ZIS/CdS-0.3 heterojunctions showed the highest activity (5.80 mmol/g), which is improved in comparison with the pure CdS (1.28 mmol/g) and ZIS (5.14 mmol/g). As already discussed, the efficiency of charge carrier separation and the acceleration of the surface reductive process in MS semiconductor photocatalysts are essential parameters in promoting photocatalytic H$_2$ evolution from water. The Ti$_3$C$_2$ (Mxene) modified all-sulfide 2D/2D S-scheme heterojunction Ti$_3$C$_2$/ZnIn$_2$S$_4$ (ZIS)/CdS composite material was produced in two steps to regulate both parameters [144]. It was demonstrated that the produced S-scheme heterojunction enhances electron-hole separation efficiency (see Figure 6 for S-scheme photocatalysts). In contrast, the intimate 2D/2D van der Waals structure provides a high interaction force and a wide contact area to promote charge transfer. Furthermore, the presence of 2D Ti$_3$C$_2$ provides the accumulation layer, minimizing electron and hole recombination. Consequently, the obtained Ti$_3$C$_2$/ZIS/CdS composite photocatalyst could reach to H$_2$ evolution rate of 8.93 mmol g^{-1} h^{-1}. The proposed charge transfer mechanism and obtained H$_2$ evolution rate are given in Figure 15a.
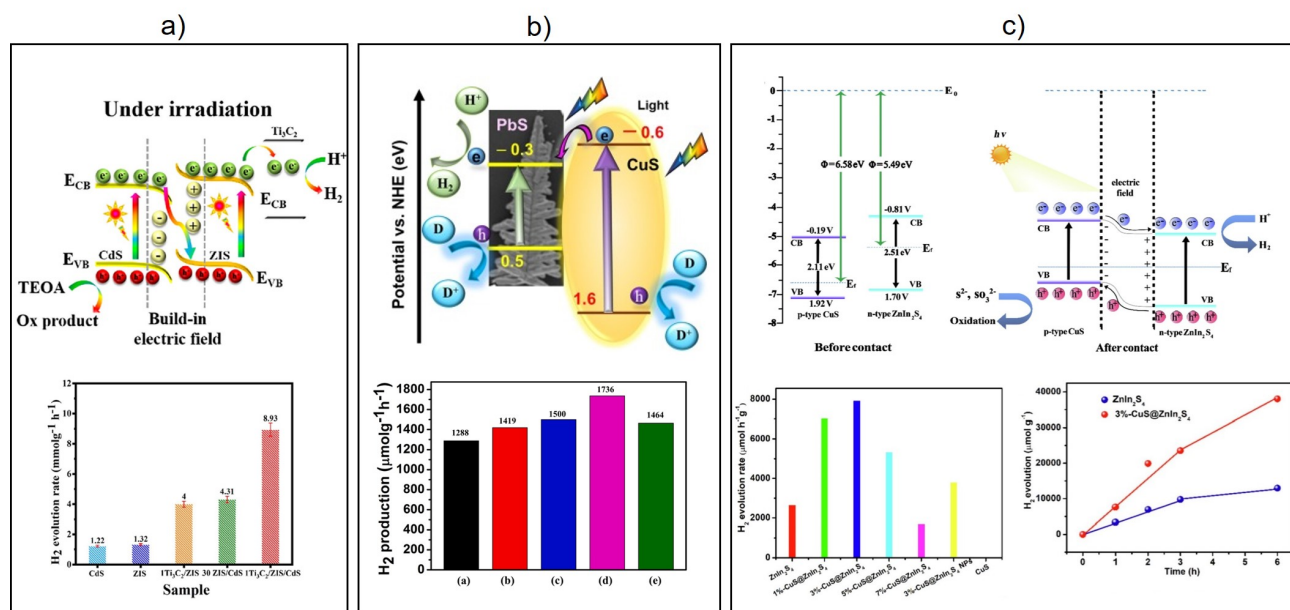
Figure 15. Photogenerated charge carrier transfer mechanisms for different MS-based hierarchical photocatalysts during the hydrogen evolution reaction. (**a**) $Zn_{1-x}Cd_xS/CdS$ [144] Copyright 2022, Elsevier. (**b**) CuS/PbS [145] Copyright 2021, Elsevier. (**c**) $CuS@ZnIn_2S_4$ [146] Copyright 2022, Elsevier. Corresponding HER plots are shown in the bottom panel. In fig (**b**) bottom axis, (**a**) corresponds to clean PbS, while (**b**–**e**) correspond to the Cu/Pb ratio of 0.414, 0.446, 0.578, 0.452, respectively.

Recently two-component co-catalyst, dendritic PbS@CuS core-shell photocatalysts were synthesized via a two-step method. Thus, a dendritic PbS core was formed through an ionic liquid/surfactant-assisted hydrothermal method synthesis, and a CuS shell was grown with an ion-exchange method [145]. In situ Cu L_3-edge near-edge X-ray-absorption fine-structure (NEXAFS) spectroscopy before and after exposure to solar light showed the photoelectron transfer from CuS to PbS. The CuS shell proportions in these dendritic PbS@CuS photocatalysts were adjusted to attain a maximal activity of 1736 mol g^{-1} h^{-1} hydrogen generation. Also, see Figure 15b for the reported HER and proposed charge transfer mechanism. Co_9S_8 is another rising member of MS photocatalysts because of its narrow band gap. Using Co_9S_8, two-component (0D)Co_9S_8/ (3D) Bi_2S_3 S-scheme heterojunction for efficient photocatalytic hydrogen evolution was reported [147]. The unique 0D/3D architecture and formed S-scheme heterojunction were shown as an efficient and convenient path for transferring photogenerated charges, which further facilitate the effective separation and diversion of the electrons. A core-shell $Cu_{1.94}S$-MnS nanosized heterostructure photocatalyst prepared via cation exchange reaction on djurleite $Cu_{1.94}S$ nanospheres template also reported exhibiting high H_2 evolution rate of 878.1 µmol g^{-1} h^{-1} [148]. In another study, CuS nanosheets-assembled hollow cubic cages were used to construct 3D hierarchical nanocages photocatalysts. Thus, 3D hierarchical nanocages $CuS@ZnIn_2S_4$ photocatalyst with abundant and compact nanosheets 2D/2D hetero-interface was designed [146]. The as prepared structure exhibited an improved photocatalytic H_2 evolution rate up to 7910 µmol g^{-1} h^{-1} in the absence of any co-catalyst. According to further experimental and theoretical studies, the strong interaction between CuS and $ZnIn_2S_4$ 2D/2D hetero-interfaces can remarkably facilitate the separation of photogenerated charge carriers and accelerate the electron transfer. The photocatalytic mechanism and optimization of HER are given in Figure 15c. The CoN with high HER performance was introduced into $Mn_{0.2}Cd_{0.8}S$ through simple electrostatic self-assembly [48]. The inclusion of CoN boosts the absorption of Vis-light by the photocatalyst. As a result of its ideal CB location and strong conductivity, CoN receives photogenerated electrons from $Mn_{0.2}Cd_{0.8}S$ as an excellent electron acceptor in the form of active sites. Remarkably, CoN significantly improved the HER of photocatalysts up to 14.612 mmol g^{-1} h^{-1}.

As stated above, one of the promising routes for photocatalytic HER enhancement is forming porous structures, which possess large surface area and enhanced excited state lifetime. However, due to the fast precipitation between the metal ions and S^{2-} ions and the large volume contraction during the sulfide formation, synthesizing such porous structures is not a straightforward process. To cope with this problem, Zhout et al. employed a general polymer-oriented acid-mediated self-assembly method to synthesize highly crystalline Mesoporous metal sulfides (MMSs) (e.g., ZnS, CdS, Ni_3S_4, CuS, and $Zn_xCd_{1-x}S$) by using polyethylenimine (PEI) as pore-forming agent [149]. The synthesis procedure, together with the structural analysis, is shown in Figure 16a–c. In order to adjust the pH and control the interactions between the inorganic precursors and the PEI, acetic acid was employed. It was found that the absorption edge of $Zn_{0.56}Cd_{0.44}S$ exhibits a slight red shift as the Cd content increases, indicating band gap narrowing. The optimized MMSs $Zn_{0.56}Cd_{0.44}S$ photocatalyst having abundant mesopores and homojunction enabled high HER of 14.3 mmol g^{-1} h^{-1}. The optimized HER plot and proposed charge transfer mechanism are shown in Figure 16d,e, respectively.
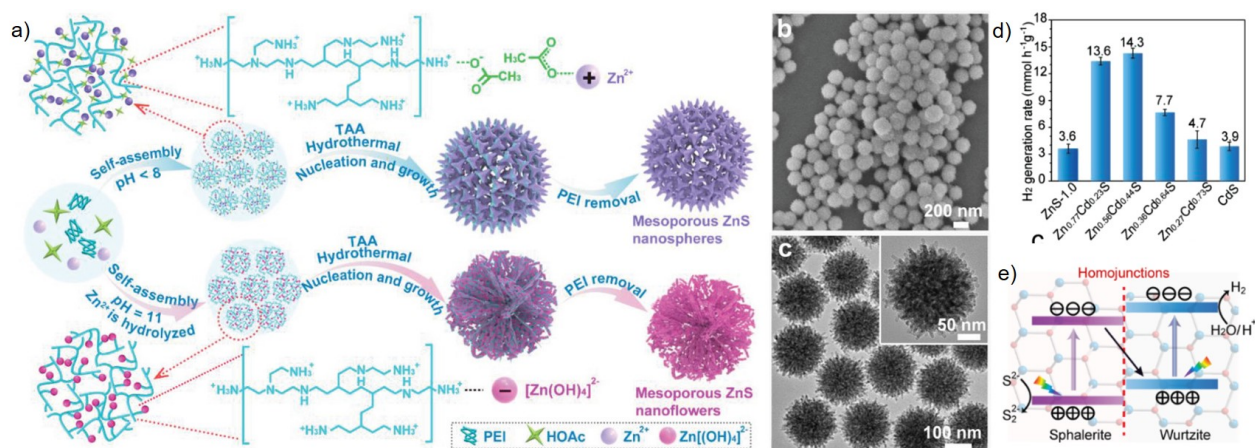

Figure 16. (**a**) Schematic illustration of the synthesis procedure of mesoporous ZnS nanostructures. (**b**,**c**) SEM and TEM images of mesoporous ZnS-1.0, respectively. (**d**) Photocatalytic HER of mesoporous $Zn_xCd_{1-x}S$ with different Cd content. (**e**) Schematic view of a photocatalytic charge transfer mechanism for mesoporous $Zn_{0.56}Cd_{0.44}$ in H_2 evolution reaction. [149] Copyright 2021, Wiley-VCH.

2.7. Plasmonic Co-Catalyst Modified Metal Sulfide Photocatalysts

Plasmons, the collective oscillation of the excited conductive charge carriers, have been in the focus of fundamental and applied sciences [150–155]. The optical response of plasmonic nanostructures can be tuned from the ultraviolet through the visible to the near-infrared wavelength, by adjusting the size, shape, composition and geometrical arrangement of the NPs. In this regard, developing new photocatalysts by employing metallic nanostructures with localized surface plasmon resonance (LSPR) is also considered state-of-the-art research. For this purpose, Au and Ag NPs are the most frequently used materials since their light absorption can effectively be shifted to Vis-light region by varying the particle size and shape [156]. In a simple picture, the enhanced electric fields around the plasmonic particle near the surface of the main MS photocatalyst increase the rate of electron-hole pair formation. As a result, the readily separated charge carriers can effectively migrate to the MS surface and drive photocatalytic process. Due to this specific pathway, combining the MS semiconductor photocatalyst with plasmonic-metal NPs can drastically reduce recombination rate. Thus, by combining enhanced light absorption capabilities through light-scattering, near-field amplification, hot-charge injection, or plasmon-induced resonance energy transfer mechanisms, such hybrid structures lead to improved photocatalytic activity and H_2 evolution rate. For example, Au-PbS-CdS nanodumbbells with double Au caps on the ends were produced using a straightforward three-step wet-chemical technique [157]. It was demonstrated that by modifying the size

and spacing of the Au caps, the LSPR-induced lateral electric field distribution surrounding the hybrid structure can be beneficially produced. Thus, the dual-plasmon-induced broad spectral coupling between the metal and semiconductor could be obtained. Moreover, multi-interface structures (e.g., PbS-CdS, Au-PbS, and Au-CdS) provide fast and multiple transfer channels for the photogenerated charges. As a result, the designed Au-PbS-CdS nanodumbbells provided photocatalytic HER of 513.63 µmol g^{-1} h^{-1}, which is superior to mixed Au, PbS, CdS NPs (97.37 µmol g^{-1} h^{-1}). Also, the CdS/TiN core-shell structure with various thicknesses of the TiN outer layer was studied [158]. The optimized heterostructure involving 15 nm TiN showed a H$_2$ production rate of 86.1 mmol g^{-1} h^{-1}, which is a 362% improvement compared to the CdS NWs. This remarkable improvement due to the TiN outer layer was assigned to a synergetic coupling of three main factors; the improvement of light absorption and electron concentration caused by LSPR, the reduction of the photo-induced carrier recombination rate, and the improved chemical stability during photocatalytic water splitting. Tu et al. have also shown that the H$_2$ evolution rate of Au NPs encapsulated by MoS$_2$ nanoflowers (Au@MoS$_2$ NFs) was remarkably improved due to the coupling of LSPR with the piezophototronic effect [159]. Consequently, applying simultaneous light illumination and mechanical vibration to the obtained structure enhanced the H$_2$ evolution rate from 2981 to 4808 µmol g^{-1} h^{-1} (see Figure 17). Thus, the piezoelectric generation of hot electrons through LSPR was a primary reason for the observed photocatalytic enhancement. The reported mechanism of the photocatalytic process involving LSPR and piezophototronic effects over the Au@MoS$_2$ NFs are described in Figure 17.
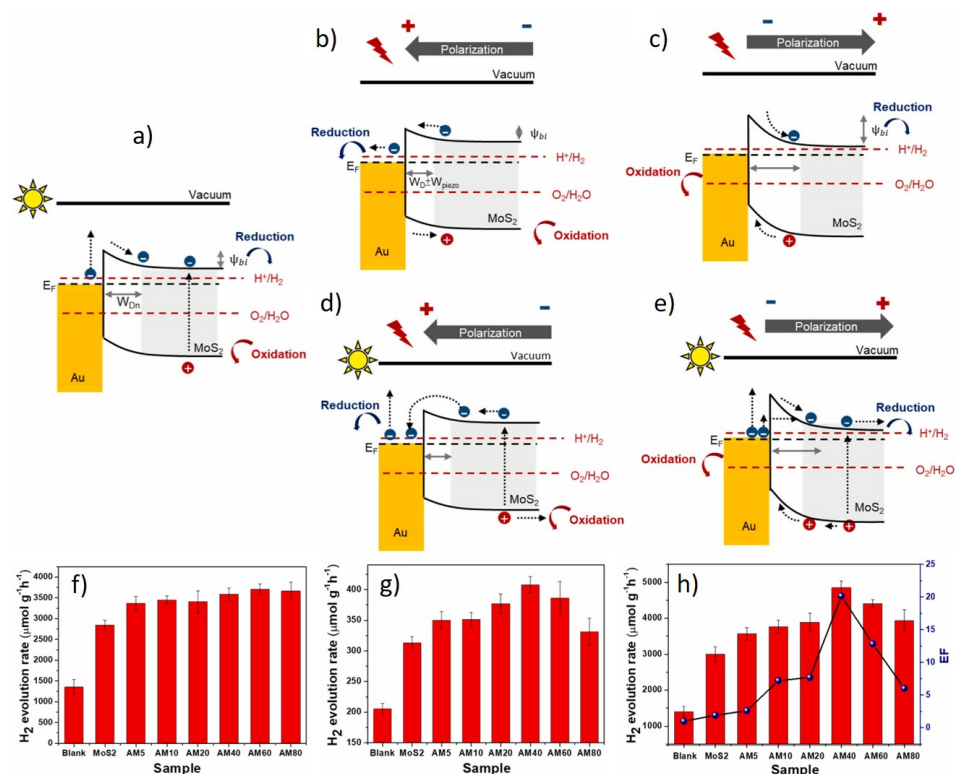
Figure 17. (**a**) The schematic representation of Au@MoS2 photocatalyst during light illumination, considering the contact between Au and MoS$_2$ with the Fermi level at equilibrium. (**b**,**c**) Au@MoS$_2$ photocatalyst under applied mechanical stress, with piezoelectric polarization point to the left side (i.e., under forwarding bias) and piezoelectric polarization point to the right side (i.e., under reverse bias), respectively. The simultaneous light illumination and ultrasonic vibration of Au@MoS$_2$ NFs with piezoelectric polarization point to the left side (**d**) and piezoelectric polarization point to the right side (**e**). The bottom panel shows the hydrogen evolution rate obtained for Au@MoS$_2$ NFs photocatalyst with different size Au NPs (i.e., 5, 10, 20, 40, 60 and 80 nm) under light irradiation (**f**), under ultrasonic vibration (**g**) and simultaneous light irradiation and ultrasonic vibration (**h**) [159]. Copyright 2021, Elsevier.

By assembling Au@CdS core-shell NPs on Ag@SiO$_2$ shell-isolated MPs dual-plasmonic-antenna nanocomposites to achieve the simultaneous efficient generation of energetic hot electrons and strong electromagnetic field enhancement for efficient photocatalytic H$_2$ evolution was reported [160]. Where, the Au@CdS antenna generates hot electrons to facilitate H$_2$ evolution reaction, while the Ag@SiO$_2$ antenna enables strong electromagnetic field enhancement to promote the generation and separation of hot carriers. The existence of both hot-electron transfer and plasmon-induced resonance energy transfer in the designed system was confirmed by transient absorption spectroscopic experiments and electromagnetic field simulations. The designed photocatalyst showed 191.2 mmol g^{-1} h^{-1} HER under Vis-light irradiation ($\lambda > 400$ nm). Cheng et al. studied modification of the Schottky barriers over Ni/S vacancy-rich Mn$_{0.3}$Cd$_{0.7}$S (Ni/MCS-s) composites prepared by the self-assembly and photochemical method [161]. The optimized Ni/MCS-s heterostructures exhibited enhanced HER up to 164.1 mmol g^{-1} h^{-1} in simulated seawater (3.5 wt% NaCl) with the maximum QYE of 60.4% at 420 nm. They showed that coupling plasmonic Ni and S vacancies can effectively lower the Schottky barrier and enhance hot electrons across the interface for the photocatalytic process. In addition, introducing the Ni layer remarkably reduced the corrosion of the catalyst in seawater. Similarly, plasmonic quaternary CuS-AgVO$_3$/Ag-TNR hetero nanostructures (HNSs) were employed to improve photocatalytic H$_2$ generation [162]. The optimized 1 wt% CuS-AgVO$_3$/Ag-TNR HNS showed the highest HER of 756 μmol g^{-1} h^{-1}. The achieved HER was related to higher charge separation, improved conductivity, LSPR, and electron-storing capacity. Au/g-C$_3$N$_4$/ZnIn$_3$S$_4$ plasma photocatalyst heterojunction composite with 3D hierarchical microarchitecture was also reported [163]. They showed that integrating Au NPs, the resulting Au/g-C$_3$N$_4$/ZnIn$_2$S$_4$ composite photocatalyst showed highest HER of 0.973 mmol g^{-1} h^{-1} under Vis-light irradiation and reached up to the maximum for the Au/g-C$_3$N$_4$ is 40 wt% of ZnIn$_2$S$_4$. In addition to the implementation of catalysts, the Zn$_{1-x}$Cr$_x$In$_2$S$_4$ solid-solution photocatalysts synthesized via a facial hydrothermal method was also reported with an improved HER [164]. The elevated HER was ascribed to the LSPR modes originating from amorphous domains, which facilitated interfacial charge transfer between amorphous and crystalline domains. Moreover, with the increase of Cr percentage in the stoichiometry, the highest photocatalytic activity ~ 7 mmol g^{-1} h^{-1} for the Z$_{0.75}$C$_{0.25}$IS after 6 hrs reaction time was achieved. This is almost 2.2 times higher than the well-known ZnIn$_2$S$_2$ photocatalyst. As already discussed, incorporating plasmonic materials with metal sulfide photocatalysts results in enhanced hydrogen production activity. Due to the fact that established control of the plasmonic signal over the spectral range and designing effective architectures remains a promising rote for further enhancement in hydrogen evolution rate. In this regard, another parameter to optimize is the amount of co-catalyst particles. Feldmann et al., for example, found that shortening the path by increasing the number of co-catalyst particles boosts the transfer rate but decreases photocatalytic performance [165]. This is due to the fact that subsequent electron transport to the acceptor is significantly slower; as a result, the recombination rate with neighboring holes increases, compensating any gain from the enhanced electron transfer rate.

3. Summary and Outlook

In this state-of-the-art review paper, we discussed very recent, namely the last two years, developments regarding metal-sulfide-based photocatalysts for H$_2$ generation. This survey showed that within a short time, a tremendous amount of effort has been devoted to this topic, which has resulted in an improvement of our fundamental understanding of the MS photocatalyzed H$_2$ production as well as a remarkable enhancement over the H$_2$ evolution rate, as summarized in Table 1. This is due to the fact that MS compounds, with their immense tunable stoichiometry, crystal structure, and electronic band structure, serve as superior research grounds over other semiconductors. Moreover, we saw that the interaction mechanism and strength of the MS with other co-catalyst and incorporated materials can easily be tuned by modifying the particle size and morphology. On the other

hand, such size reduction and corresponding controllable electronic modification make the MS materials the perfect playground for studying light-matter interaction, which is highly important for designing and developing a new generation of effective photocatalytic systems. This survey also showed that in addition to the new emerging photocatalysts, the conventional ones also still require more studies and stay promising for vast-scale application. Especially promising is combining such well-known photocatalysts with porous materials to overcome the short excited state lifetime and enhance the light absorption capability. Evidently, hierarchical nanostructured are also promising photocatalysts for H_2 evolution, which however investigated only in a limited manner and materials. Hence, more research is required in order to find suitable co-catalysts, to optimize nanostructural morphology and finding suitable doping agent to enhance light absorption range. In this regard, developing photocatalytsts with earth-abundant metal based co-catalysts (such as NiS_2, MoS_2, CuS, etc.) and nobel metal-free co-catalysts should be more prioritized. Moreover, building hierarchical structures based on low-dimensional and metal free materials such as graphene, g-CN, graphene oxide, etc. is more promising also to reduce metal contamination and production cost. Another interesting and very promising photocatalytic systems would be membrane systems having advantage of photocatalysis and membrane separation. Eventually, a better understanding of charge generation, separation, and transport through the photocatalytic process, reactions at the surface, interaction of heterogeneous photocatalyst with the environment is necessary to design stable photocatalysts with an enhanced performance towards scalable applications. One of the most important researches in this direction should be developing facile, controllable and cost effective synthesis methods for photocatalytic systems.

Table 1. Summary of recently reported metal sulfide based photocatalysts with improved efficiency for the H_2 evolution.

Photocatalyst	Type/Junction	Rate (μmol g^{-1} h^{-1})	QYE (%)	Incident Light (λ, nm)	Ref.
WN/CdS	Schottky (p-n)	24,130	19.8	>420	[55]
CdS@Ni$_2$P	n-n	287	-	480	[53]
NiWO$_4$/CdS nanosheets	Z-scheme	26,430	22	420	[54]
PtP$_2$@C/CdS (10 wt%)	-	9760	41.67	420	[56]
3 wt% WC/CdS	Schottky	9180	14.3	420	[59]
red-P/Co$_9$S$_8$	Schottky	4362	-	UV-Vis	[119]
25 wt%-ZnCo$_2$S$_4$4/g-C$_3$N$_4$	S-scheme	6619	-	Lab-solar	[120]
CuNiS/g-C$_3$N$_4$	p-n	752.8	-	800	[121]
T-COF/CdS	Z-scheme	500	37.8	365	[122]
Mn$_{0.2}$Cd$_{0.8}$S/Ni-MOF-74	type-II	7104		>420	[123]
CdS@NiS/MOFs	p-n	42,700	13.23	450	[124]
ZnCdS/UIO-66(Ce)	type-II	3958	-	UV-Vis	[125]
ZnIn$_2$S$_4$-MOF layer	-	28,200	22.67	350	[126]
Pt@NH$_2$-UiO-66/CdS	type-II	38,000	40.3	400	[127]
CN/amorphous-MoS$_2$/Pt	Schottky	5830	8.51	400	[107]
CoS$_x$-rGO/TiO$_2$ (10%)	-	256.97	14.62	365	[98]

Table 1. *Cont.*

Photocatalyst	Type/Junction	Rate (μmol g^{-1} h^{-1})	QYE (%)	Incident Light (λ, nm)	Ref.
TiO$_2$@CuS	LSPR-Schottky	2467	13.4/3.7	UV-vis/near-IR	[99]
BiS$_x$/TiO$_2$ (1.0 wt%)	-	803.2	3.86	365	[100]
NiWS$_x$-ND/TiO$_2$ (3 wt%)	Schottky	4580	13	365	[103]
ZnCo$_2$S$_4$/TiO$_2$	S-scheme	5580	11.5	420	[104]
amorphous MoO$_2$/TiO$_2$	co-catalyst	880.3	-	UV-Vis	[105]
TiO$_2$-ZnIn$_2$S$_4$	direct Z-scheme	214.9	36.7/11.6	UV/Vis	[106]
MoS$_2$/Fe$_2$O$_3$/g-C$_3$N$_4$	Z-scheme	7820	-	Vis	[109]
Co$_3$S$_4$/g-CN	Ohmic	536.0	7.55	400	[111]
NiS@g-C$_3$N$_4$-30	co-catalyst	3297	-	Vis	[42]
NiS/g-C$_3$N$_4$	co-catalyst	244	-	420	[112]
PtS/g-C$_3$N$_4$ nanosheets	co-catalyst	1072.6	45.7	420	[113]
Pt/MoS$_2$/g-C$_3$N$_4$	co-catalyst	1595.3	30.9	435	[114]
ZnS-NiS$_2$/g-C$_3$N$_4$	dual co-catalyst	302.7	1.8	>420	[115]
2D SnS/g-C$_3$N$_4$ nanosheets	Z-scheme	818.93	0.55	Solar-simulator	[116]
Ni$_x$PB-rGO/CdS	p-n	5790	9	420	[52]
MoS$_2$ /ZnIn$_2$S$_4$	co-catalyst	221.71	11.8	420	[134]
CdS-SV@CuS(5%)	-	1654.53	6.51	450	[137]
W$_{18}$O$_{49}$/Cd$_{0.5}$Zn$_{0.5}$S	S-scheme	147,700	45.3	<460	[166]
MoS$_2$@MoO$_3$	S-scheme	12,416.8	8.43	500	[92]
CdSe/CuInS$_2$ microflowers	p-n	10,610.37	48.97	420	[72]
3% Ni-doped Mn$_{0.5}$Cd$_{0.5}$S	-	108,300	-	420	[73]
a-NiCuS$_x$/TiO$_2$ (3:1)	-	427.9	34.67	UV	[167]
Co$_9$S$_8$@CdIn$_2$S$_4$	type-I	4604	-	Vis	[47]

References

1. United Nations. Sustainable Development Goals. 2021. Available online: www.un.org (accessed on 27 September 2022).
2. Bonde, J.; Moses, P.G.; Jaramillo, T.F.; Nørskov, J.K.; Chorkendorff, I. Hydrogen evolution on nano-particulate transition metal sulfides. *Faraday Discuss.* **2009**, *140*, 219–231. [CrossRef]
3. Mamiyev, Z.Q.; Balayeva, N.O. Preparation and optical studies of PbS nanoparticles. *Opt. Mater.* **2015**, *46*, 522–525. [CrossRef]
4. Ganapathy, M.; Chang, C.T.; Alagan, V. Facile preparation of amorphous SrTiO$_3$-crystalline PbS heterojunction for efficient photocatalytic hydrogen production. *Int. J. Hydrogen Energy* **2022**, *47*, 27555–27565. [CrossRef]
5. Maeda, K.; Teramura, K.; Lu, D.; Takata, T.; Saito, N.; Inoue, Y.; Domen, K. Photocatalyst releasing hydrogen from water. *Nature* **2006**, *440*, 295. [CrossRef] [PubMed]
6. Balayeva, N.O.; Mamiyev, Z.Q. Synthesis and characterization of Ag$_2$S/PVA-fullerene (C60) nanocomposites. *Mater. Lett.* **2016**, *175*, 231–235. [CrossRef]
7. Baran, T.; Wojtyła, S.; Dibenedetto, A.; Aresta, M.; Macyk, W. Zinc sulfide functionalized with ruthenium nanoparticles for photocatalytic reduction of CO$_2$. *Appl. Catal. B* **2015**, *178*, 170–176. [CrossRef]
8. Frame, F.A.; Osterloh, F.E. CdSe-MoS$_2$: A Quantum Size-Confined Photocatalyst for Hydrogen Evolution from Water under Visible Light. *J. Phys. Chem. C* **2010**, *114*, 10628–10633. [CrossRef]
9. Keimer, B.; Moore, J. The physics of quantum materials. *Nat. Phys.* **2017**, *13*, 1045–1055. [CrossRef]

10. Sivula, K.; Van De Krol, R. Semiconducting materials for photoelectrochemical energy conversion. *Nat. Rev. Mater.* **2016**, *1*, 15010. [CrossRef]

11. Amirav, L.; Alivisatos, A.P. Photocatalytic Hydrogen Production with Tunable Nanorod Heterostructures. *J. Phys. Chem. Lett.* **2010**, *1*, 1051–1054. [CrossRef]

12. Shiga, Y.; Umezawa, N.; Srinivasan, N.; Koyasu, S.; Sakai, E.; Miyauchi, M. A metal sulfide photocatalyst composed of ubiquitous elements for solar hydrogen production. *Chem. Commun.* **2016**, *52*, 7470–7473. [CrossRef]

13. Hou, H.; Yuan, Y.; Cao, S.; Yang, Y.; Ye, X.; Yang, W. $CuInS_2$ nanoparticles embedded in mesoporous TiO_2 nanofibers for boosted photocatalytic hydrogen production. *J. Mater. Chem. C* **2020**, *8*, 11001–11007. [CrossRef]

14. Caudillo-Flores, U.; Kubacka, A.; Berestok, T.; Zhang, T.; Llorca, J.; Arbiol, J.; Cabot, A.; Fernández-García, M. Hydrogen photogeneration using ternary $CuGaS_2$-TiO_2-Pt nanocomposites. *Int. J. Hydrogen Energy* **2020**, *45*, 1510–1520. [CrossRef]

15. Singh, J.; Soni, R. Enhanced sunlight driven photocatalytic activity of In_2S_3 nanosheets functionalized MoS_2 nanoflowers heterostructures. *Sci. Rep.* **2021**, *11*, 15352. [CrossRef] [PubMed]

16. Wojtyła, S.; Baran, T. Photocatalytic H_2 production over RuO_2@ZnS and RuO_2@CuS nanostructures. *Int. J. Hydrogen Energy* **2019**, *44*, 14624–14634. [CrossRef]

17. Liu, Y.; Meng, X.; Wang, Z.; Qiu, J. A Li_2S-based all-solid-state battery with high energy and superior safety. *Sci. Adv.* **2022**, *8*, eabl8390. [CrossRef]

18. Balayeva, N.O.; Mamiyev, Z. Integrated processes involving adsorption, photolysis, and photocatalysis. In *Hybrid and Combined Processes for Air Pollution Control*; Elsevier: Amsterdam, The Netherlands, 2022; pp. 117–153. [CrossRef]

19. Jiang, B.; Guo, Y.; Kim, J.; Whitten, A.E.; Wood, K.; Kani, K.; Rowan, A.E.; Henzie, J.; Yamauchi, Y. Mesoporous Metallic Iridium Nanosheets. *J. Am. Chem. Soc.* **2018**, *140*, 12434–12441. [CrossRef]

20. Lee, Y.Y.; Jung, H.S.; Kim, J.M.; Kang, Y.T. Photocatalytic CO_2 conversion on highly ordered mesoporous materials: Comparisons of metal oxides and compound semiconductors. *Appl. Catal. B* **2018**, *224*, 594–601. [CrossRef]

21. Tang, J.; Durrant, J.R.; Klug, D.R. Mechanism of Photocatalytic Water Splitting in TiO2. Reaction of Water with Photoholes, Importance of Charge Carrier Dynamics, and Evidence for Four-Hole Chemistry. *J. Am. Chem. Soc.* **2008**, *130*, 13885–13891. [CrossRef]

22. Meerbach, C.; Klemmed, B.; Spittel, D.; Bauer, C.; Park, Y.J.; Hubner, R.; Jeong, H.Y.; Erb, D.; Shin, H.S.; Lesnyak, V.; et al. General colloidal synthesis of transition-metal disulfide nanomaterials as electrocatalysts for hydrogen evolution reaction. *ACS Appl. Mater. Interfaces* **2020**, *12*, 13148–13155. [CrossRef] [PubMed]

23. Mamiyev, Z.Q.; Balayeva, N.O. CuS nanoparticles synthesized by a facile chemical route under different pH conditions. *Mendeleev Commun.* **2016**, *26*, 235–237. [CrossRef]

24. Devi, S.A.; Singh, K.J.; Devi, K.N. Visible light driven photocatalytic activities of metal sulfides synthesized by simple co-precipitation method. *Mater. Today Proc.* **2022**, *65*, 2819–2824. [CrossRef]

25. Zhang, Y.; Han, L.; Wang, C.; Wang, W.; Ling, T.; Yang, J.; Dong, C.; Lin, F.; Du, X.W. Zinc-Blende CdS Nanocubes with Coordinated Facets for Photocatalytic Water Splitting. *ACS Catal.* **2017**, *7*, 1470–1477. [CrossRef]

26. Wu, K.; Rodríguez-Córdoba, W.E.; Liu, Z.; Zhu, H.; Lian, T. Beyond Band Alignment: Hole Localization Driven Formation of Three Spatially Separated Long-Lived Exciton States in CdSe/CdS Nanorods. *ACS Nano* **2013**, *7*, 7173–7185. [CrossRef] [PubMed]

27. Li, H.; Gao, Y.; Zhou, Y.; Fan, F.; Han, Q.; Xu, Q.; Wang, X.; Xiao, M.; Li, C.; Zou, Z. Construction and Nanoscale Detection of Interfacial Charge Transfer of Elegant Z-Scheme WO_3/Au/In_2S_3 Nanowire Arrays. *Nano Lett.* **2016**, *16*, 5547–5552. [CrossRef] [PubMed]

28. Shown, I.; Samireddi, S.; Chang, Y.C.; Putikam, R.; Chang, P.H.; Sabbah, A.; Fu, F.Y.; Chen, W.F.; Wu, C.I.; Yu, T.Y.; et al. Carbon-doped SnS_2 nanostructure as a high-efficiency solar fuel catalyst under visible light. *Nat. Commun* **2018**, *9*, 169. [CrossRef]

29. Wang, S.; Guan, B.Y.; Lou, X.W.D. Construction of $ZnIn_2S_4$-In_2O_3 Hierarchical Tubular Heterostructures for Efficient CO_2 Photoreduction. *J. Am. Chem. Soc.* **2018**, *140*, 5037–5040. [CrossRef] [PubMed]

30. Sun, S.; An, Q.; Watanabe, M.; Cheng, J.; Ho Kim, H.; Akbay, T.; Takagaki, A.; Ishihara, T. Highly correlation of CO_2 reduction selectivity and surface electron Accumulation: A case study of Au-MoS_2 and Ag-MoS_2 catalyst. *Appl. Catal. B* **2020**, *271*, 118931. [CrossRef]

31. Li, P.; Zhang, X.; Hou, C.; Chen, Y.; He, T. Highly efficient visible-light driven solar-fuel production over tetra(4-carboxyphenyl)porphyrin iron(III) chloride using CdS/Bi_2S_3 heterostructure as photosensitizer. *Appl. Catal. B* **2018**, *238*, 656–663. [CrossRef]

32. Huang, L.; Li, B.; Su, B.; Xiong, Z.; Zhang, C.; Hou, Y.; Ding, Z.; Wang, S. Fabrication of hierarchical Co_3O_4@ $CdIn_2S_4$ p–n heterojunction photocatalysts for improved CO_2 reduction with visible light. *J. Mater. Chem. A* **2020**, *8*, 7177–7183. [CrossRef]

33. Deng, F.; Lu, X.; Luo, Y.; Wang, J.; Che, W.; Yang, R.; Luo, X.; Luo, S.; Dionysiou, D.D. Novel visible-light-driven direct Z-scheme CdS/$CuInS_2$ nanoplates for excellent photocatalytic degradation performance and highly-efficient Cr(VI) reduction. *J. Chem. Eng.* **2019**, *361*, 1451–1461. [CrossRef]

34. Zhou, M.; Wang, S.; Yang, P.; Huang, C.; Wang, X. Boron Carbon Nitride Semiconductors Decorated with CdS Nanoparticles for Photocatalytic Reduction of CO_2. *ACS Catal.* **2018**, *8*, 4928–4936. [CrossRef]

35. Raza, A.; Shen, H.; Haidry, A.A. Novel Cu_2ZnSnS_4/Pt/g-C_3N_4 heterojunction photocatalyst with straddling band configuration for enhanced solar to fuel conversion. *Appl. Catal. B* **2020**, *277*, 119239. [CrossRef]

36. Wu, S.; Pang, H.; Zhou, W.; Yang, B.; Meng, X.; Qiu, X.; Chen, G.; Zhang, L.; Wang, S.; Liu, X.; et al. Stabilizing $CuGaS_2$ by crystalline CdS through an interfacial Z-scheme charge transfer for enhanced photocatalytic CO_2 reduction under visible light. *Nanoscale* **2020**, *12*, 8693–8700. [CrossRef] [PubMed]

37. Li, X.; Sun, Y.; Xu, J.; Shao, Y.; Wu, J.; Xu, X.; Pan, Y.; Ju, H.; Zhu, J.; Xie, Y. Selective visible-light-driven photocatalytic CO_2 reduction to CH_4 mediated by atomically thin $CuIn_5S_8$ layers. *Nat. Energy* **2019**, *4*, 690–699. [CrossRef]

38. Kočí, K.; Matějová, L.; Kozák, O.; Čapek, L.; Valeš, V.; Reli, M.; Praus, P.; Šafářová, K.; Kotarba, A.; Obalová, L. ZnS/MMT nanocomposites: The effect of ZnS loading in MMT on the photocatalytic reduction of carbon dioxide. *Appl. Catal. B* **2014**, *158–159*, 410–417. [CrossRef]

39. Sharma, N.; Das, T.; Kumar, S.; Bhosale, R.; Kabir, M.; Ogale, S. Photocatalytic Activation and Reduction of CO_2 to CH_4 over Single Phase Nano Cu_3SnS_4: A Combined Experimental and Theoretical Study. *ACS Appl. Energy Mater.* **2019**, *2*, 5677–5685. [CrossRef]

40. Guo, Y.; Ao, Y.; Wang, P.; Wang, C. Mediator-free direct dual-Z-scheme $Bi_2S_3/BiVO_4/MgIn_2S_4$ composite photocatalysts with enhanced visible-light-driven performance towards carbamazepine degradation. *Appl. Catal. B* **2019**, *254*, 479–490. [CrossRef]

41. Zeng, R.; Lian, K.; Su, B.; Lu, L.; Lin, J.; Tang, D.; Lin, S.; Wang, X. Versatile synthesis of hollow metal sulfides via reverse cation exchange reactions for photocatalytic CO_2 reduction. *Angew. Chem. Int. Ed.* **2021**, *60*, 25055–25062. [CrossRef]

42. Chen, L.; Yang, Z.; Chen, B. Uniformly Dispersed Metal Sulfide Nanodots on g-C_3N_4 as Bifunctional Catalysts for High-Efficiency Photocatalytic H_2 and H_2O_2 Production under Visible-Light Irradiation. *Energy Fuels* **2021**, *35*, 10746–10755. [CrossRef]

43. Liu, H.; Tan, P.; Liu, Y.; Zhai, H.; Du, W.; Liu, X.; Pan, J. Ultrafast interfacial charge evolution of the Type-II cadmium Sulfide/Molybdenum disulfide heterostructure for photocatalytic hydrogen production. *J. Colloid Interface Sci.* **2022**, *619*, 246–256. [CrossRef] [PubMed]

44. Ma, X.; Li, D.; Su, P.; Jiang, Z.; Jin, Z. S-scheme $W_{18}O_{49}/Mn_{0.2}Cd_{0.8}S$ Heterojunction for Improved Photocatalytic Hydrogen Evolution. *ChemCatChem* **2021**, *13*, 2179–2190. [CrossRef]

45. Tada, H.; Mitsui, T.; Kiyonaga, T.; Akita, T.; Tanaka, K. All-solid-state Z-scheme in CdS–Au–TiO_2 three-component nanojunction system. *Nat. Mater.* **2006**, *5*, 782–786. [CrossRef] [PubMed]

46. Balayeva, N.O.; Mamiyev, Z.Q. Synthesis and studies of CdS and ZnS-PE/NBR modified thermoplastic elastomeric copolymer nanocomposite films. *Mater. Lett.* **2016**, *162*, 121–125. [CrossRef]

47. Yendrapati, T.P.; Soumya, J.; Bojja, S.; Pal, U. Robust $Co_9S_8@CdIn_2S_4$ cage for efficient photocatalytic H_2 evolution. *J. Phys. Chem. C* **2021**, *125*, 5099–5109. [CrossRef]

48. Gong, H.; Hao, X.; Li, H.; Jin, Z. A novel materials manganese cadmium sulfide/cobalt nitride for efficiently photocatalytic hydrogen evolution. *J. Colloid Interface Sci.* **2021**, *585*, 217–228. [CrossRef]

49. Wang, Y.; Chen, X.; Chen, C. Microwave synthesis of Zn, Cd binary metal sulfides with superior photocatalytic H_2 evolution performance. *Inorg. Chem Commun.* **2021**, *134*, 108993. [CrossRef]

50. Xu, L.; Zhang, S.Z.; Li, W.; Zhang, Z.H. Visible-Light-Mediated Oxidative Amidation of Aldehydes by Using Magnetic CdS Quantum Dots as a Photocatalyst. *Chem. Eur. J.* **2021**, *27*, 5483–5491. [CrossRef]

51. Mamiyev, Z.Q.; Balayeva, N.O. Synthesis and characterization of CdS nanocrystals and maleic anhydride octene-1 copolymer nanocomposite materials by the chemical in-situ technique. *Compos. B. Eng.* **2015**, *68*, 431–435. [CrossRef]

52. Long, H.; Wang, P.; Wang, X.; Chen, F.; Yu, H. Optimizing hydrogen adsorption of Ni_xB cocatalyst by integrating P atom for enhanced photocatalytic H_2-production activity of CdS. *Appl. Surf. Sci.* **2022**, *604*, 154457. [CrossRef]

53. Li, K.; Chen, X.; Zhao, J.; She, H.; Huang, J.; Wang, L.; Wang, Q. Photodeposition Synthesis of CdS@Ni_2P Composites for Efficacious Photocatalytic Hydrogen Evolution. *ACS Appl. Energy Mater.* **2022**, *5*, 10207–10215. [CrossRef]

54. Yin, X.L.; Li, L.L.; Gao, G.M.; Lu, Y.; Shang, Q.Q.; Zhao, H.T.; Li, D.C.; Dou, J.M. Direct Z-Scheme $NiWO_4$/CdS nanosheets-on-nanorods nanoheterostructure for efficient visible-light-driven H_2 generation. *Int. J. Hydrogen Energy* **2022**, *47*, 9895–9904. [CrossRef]

55. Liu, H.; Chen, J.; Guo, W.; Xu, Q.; Min, Y. A high efficiency water hydrogen production method based on CdS/WN composite photocatalytic. *J. Colloid Interface Sci.* **2022**, *613*, 652–660. [CrossRef] [PubMed]

56. Xu, J.; Zhong, W.; Gao, D.; Wang, X.; Wang, P.; Yu, H. Phosphorus-enriched platinum diphosphide nanodots as a highly efficient cocatalyst for photocatalytic H_2 evolution of CdS. *J. Chem. Eng.* **2022**, *439*, 135758. [CrossRef]

57. Lin, Q.; Liang, S.; Wang, J.; Zhang, R.; Wang, X. Cadmium Sulfide 3D Photonic Crystal with Hierarchically Ordered Macropores for Highly Efficient Photocatalytic Hydrogen Generation. *Inorg. Chem.* **2022**, *61*, 2920–2928. [CrossRef]

58. Luan, X.; Dai, H.; Li, Q.; Xu, F.; Mai, Y. A Hybrid Photocatalyst Composed of CdS Nanoparticles and Graphene Nanoribbons for Visible-Light-Driven Hydrogen Production. *ACS Appl. Energy Mater.* **2022**, *5*, 8621–8628. [CrossRef]

59. Lei, Y.; Ng, K.H.; Zhang, Y.; Li, Z.; Xu, S.; Huang, J.; Lai, Y. One-pot loading of cadmium sulfide onto tungsten carbide for efficient photocatalytic H_2 evolution under visible light irradiation. *J. Chem. Eng.* **2022**, *434*, 134689. [CrossRef]

60. Cao, X.; Zhang, L.; Guo, C.; Chen, T.; Feng, C.; Liu, Z.; Qi, Y.; Wang, W.; Wang, J. Ni-doped CdS porous cubes prepared from prussian blue nanoarchitectonics with enhanced photocatalytic hydrogen evolution performance. *Int. J. Hydrogen Energy* **2022**, *47*, 3752–3761. [CrossRef]

61. Gao, D.; Xu, J.; Wang, L.; Zhu, B.; Yu, H.; Yu, J. Optimizing Atomic Hydrogen Desorption of Sulfur-Rich NiS_{1+x} Cocatalyst for Boosting Photocatalytic H_2 Evolution. *Adv. Mater.* **2022**, *34*, 2108475. [CrossRef]

62. Balayeva, O.O.; Azizov, A.A.; Muradov, M.B.; Maharramov, A.M.; Eyvazova, G.M.; Alosmanov, R.M.; Mamiyev, Z.Q.; Aghamaliyev, Z.A. *β*-NiS and Ni₃S₄ nanostructures: Fabrication and characterization. *Mater. Res. Bull.* **2016**, *75*, 155–161. [CrossRef]

63. Muniyappa, M.; Kalegowda, S.N.; Shetty, M.; Sriramoju, J.B.; Shastri, M.; Rao, S.V.N.; De, D.; Shankar, M.V.; Rangappa, D. Cocatalyst free nickel sulphide nanostructure for enhanced photocatalytic hydrogen evolution. *Int. J. Hydrogen Energy* **2022**, *47*, 5307–5318. [CrossRef]

64. Zhang, M.; Chen, X.; Jiang, X.; Wang, J.; Xu, L.; Qiu, J.; Lu, W.; Chen, D.; Li, Z. Activate Fe₃S₄ nanorods by Ni doping for efficient dye-sensitized photocatalytic hydrogen production. *ACS Appl. Mater.* **2021**, *13*, 14198–14206. [CrossRef]

65. Sarilmaz, A.; Yanalak, G.; Aslan, E.; Ozel, F.; Patir, I.H.; Ersoz, M. Shape-controlled synthesis of copper based multinary sulfide catalysts for enhanced photocatalytic hydrogen evolution. *Renew. Energy* **2021**, *164*, 254–259. [CrossRef]

66. Praveen Kumar, D.; Rangappa, A.P.; Kim, S.; Kim, E.; Reddy, K.A.J.; Gopannagari, M.; Bhavani, P.; Reddy, D.A.; Kim, T.K. Boosting charge transfers in cadmium sulfide nanorods with a few layered Ni-doped MoS₂ nanosheets for enhanced photocatalytic hydrogen evolution. *Int. J. Hydrogen Energy* 2022, *in press*. [CrossRef]

67. Tao, C.L.; Xie, Z.; Xu, D.; Li, X.; Ge, F.; Chen, F.; Jiang, Z.; Gu, W.; Cheng, F.; Wu, X.J. Templated Synthesis of Ultrathin Indium-Based Ternary Metal Sulfide (MIn₂S₄, M = Zn, Cd, and Ni) Nanoplates for Photocatalytic Hydrogen Evolution. *ACS Appl. Energy Mater.* **2022**, *5*, 4877–4884. [CrossRef]

68. Pan, R.; Hu, M.; Liu, J.; Li, D.; Wan, X.; Wang, H.; Li, Y.; Zhang, X.; Wang, X.; Jiang, J.; et al. Two-dimensional all-in-one sulfide monolayers driving photocatalytic overall water splitting. *Nano Lett.* **2021**, *21*, 6228–6236. [CrossRef]

69. Lei, Y.; Zhang, Y.; Li, Z.; Xu, S.; Huang, J.; Ng, K.H.; Lai, Y. Molybdenum sulfide cocatalyst activation upon photodeposition of cobalt for improved photocatalytic hydrogen production activity of ZnCdS. *J. Chem. Eng.* **2021**, *425*, 131478. [CrossRef]

70. Zhong, W.; Gao, D.; Yu, H.; Fan, J.; Yu, J. Novel amorphous NiCuSₓ H₂-evolution cocatalyst: Optimizing surface hydrogen desorption for efficient photocatalytic activity. *J. Chem. Eng.* **2021**, *419*, 129652. [CrossRef]

71. Xu, W.; Xie, Z.; Han, W.; Zhang, K.; Guo, D.; Chang, K. Rational design of interfacial energy level matching for CuGaS₂ based photocatalysts over hydrogen evolution reaction. *Int. J. Hydrogen Energy* **2022**, *47*, 11853–11862. [CrossRef]

72. Wang, Y.; Peng, J.; Xu, Y.; Zhao, R.; Han, J.; Wang, L. Facile fabrication of CdSe/CuInS₂ microflowers with efficient photocatalytic hydrogen production activity. *Int. J. Hydrogen Energy* **2022**, *47*, 8294–8302. [CrossRef]

73. Feng, K.; Wang, C.; Hu, X.; Fan, J.; Liu, E. Highly efficient photocatalytic H₂ evolution over Ni-doped Mn₀.₅Cd₀.₅S nanorods under visible light. *Int. J. Energy Res.* **2022**, *46*, 20828–20837. [CrossRef]

74. Liu, W.; Chen, J.; Pan, X.; Wang, T.; Li, Y. Ultrathin Nickel-doped ZnIn₂S₄ Nanosheets with Sulfur Vacancies for Efficient Photocatalytic Hydrogen Evolution. *ChemCatChem* **2021**, *13*, 5148–5155. [CrossRef]

75. Hou, T.; Liang, J.; Wang, L.; Zheng, Z.; Wang, J.; Xing, X.; Tang, H.; Zeng, C.; Wang, B. Cd₁₋ₓZnₓS biomineralized by engineered bacterium for efficient photocatalytic hydrogen production. *Mater. Today Energy* **2021**, *22*, 100869. [CrossRef]

76. Li, F.; Jiang, J.; Li, N.; Gao, Y.; Ge, L. Design and fabrication of hollow structured Cu₂MoS₄/ZnIn₂S₄ nanocubes with significant enhanced photocatalytic hydrogen evolution performance. *Int. J. Hydrogen Energy* **2021**, *46*, 37847–37859. [CrossRef]

77. Raja, A.; Son, N.; Swaminathan, M.; Kang, M. Facile synthesis of sphere-like structured ZnIn₂S₄-rGO-CuInS₂ ternary heterojunction catalyst for efficient visible-active photocatalytic hydrogen evolution. *J. Colloid Interface Sci.* **2021**, *602*, 669–679. [CrossRef]

78. Chong, W.K.; Ng, B.J.; Er, C.C.; Tan, L.L.; Chai, S.P. Insights from density functional theory calculations on heteroatom P-doped ZnIn₂S₄ bilayer nanosheets with atomic-level charge steering for photocatalytic water splitting. *Sci. Rep.* **2022**, *12*, 1927. [CrossRef] [PubMed]

79. Lin, B.; Chen, H.; Zhou, Y.; Luo, X.; Tian, D.; Yan, X.; Duan, R.; Di, J.; Kang, L.; Zhou, A.; et al. 2D/2D atomic double-layer WS₂/Nb₂O₅ shell/core nanosheets with ultrafast interfacial charge transfer for boosting photocatalytic H₂ evolution. *Chin. Chem. Lett.* **2021**, *32*, 3128–3132. [CrossRef]

80. Ren, X.; Shi, J.; Duan, R.; Di, J.; Xue, C.; Luo, X.; Liu, Q.; Xia, M.; Lin, B.; Tang, W. Construction of high-efficiency CoS@Nb₂O₅ heterojunctions accelerating charge transfer for boosting photocatalytic hydrogen evolution. *Chin. Chem. Lett.* **2022**, *33*, 4700–4704. [CrossRef]

81. Li, J.; Li, M.; Li, Y.; Guo, X.; Jin, Z. Lotus-leaf-like Bi₂O₂CO₃ nanosheet combined with MO₂S₃ for higher photocatalytic hydrogen evolution. *Sep. Purif. Technol.* **2022**, *288*, 120588. [CrossRef]

82. Sun, M.; Zhang, Z.; Shi, Q.; Yang, J.; Xie, M.; Han, W. Toward photocatalytic hydrogen generation over BiVO₄ by controlling particle size. *Chin. Chem. Lett.* **2021**, *32*, 2419–2422. [CrossRef]

83. Gogoi, D.; Shah, A.K.; Rambabu, P.; Qureshi, M.; Golder, A.K.; Peela, N.R. Step-Scheme Heterojunction between CdS Nanowires and Facet-Selective Assembly of MnOₓ-BiVO₄ for an Efficient Visible-Light-Driven Overall Water Splitting. *ACS Appl. Mater. Interfaces* **2021**, *13*, 45475–45487. [CrossRef]

84. Iwase, A.; Yoshino, S.; Takayama, T.; Ng, Y.H.; Amal, R.; Kudo, A. Water Splitting and CO₂ Reduction under Visible Light Irradiation Using Z-Scheme Systems Consisting of Metal Sulfides, CoOₓ-Loaded BiVO₄, and a Reduced Graphene Oxide Electron Mediator. *J. Am. Chem. Soc.* **2016**, *138*, 10260–10264. [CrossRef]

85. Ghouri, M.; Ahmed, E.; Ali, A.; Ramzan, M.; Irfan, M. Improved photocatalytic H₂ evolution over composites based on niobium pentoxide, metal sulfides and graphene. *Mater. Sci. Semicond. Process.* **2021**, *122*, 105492. [CrossRef]

86. Liu, M.; Li, P.; Wang, S.; Liu, Y.; Zhang, J.; Chen, L.; Wang, J.; Liu, Y.; Shen, Q.; Qu, P.; et al. Hierarchically porous hydrangea-like In_2S_3/In_2O_3 heterostructures for enhanced photocatalytic hydrogen evolution. *J. Colloid Interface Sci.* **2021**, *587*, 876–882. [CrossRef] [PubMed]

87. Li, Q.; Lu, Q.; Guo, E.; Wei, M.; Pang, Y. Hierarchical $Co_9S_8/ZnIn_2S_4$ Nanoflower Enables Enhanced Hydrogen Evolution Photocatalysis. *Energy Fuels* **2022**, *36*, 4541–4548. [CrossRef]

88. Xiang, D.; Hao, X.; Jin, Z. Cu/CdS/MnOx Nanostructure-Based Photocatalyst for Photocatalytic Hydrogen Evolution. *ACS Appl. Nano Mater.* **2021**, *4*, 13848–13860. [CrossRef]

89. Khanal, V.; Balayeva, N.O.; Günnemann, C.; Mamiyev, Z.; Dillert, R.; Bahnemann, D.W.; Subramanian, V.R. Photocatalytic NO_x removal using tantalum oxide nanoparticles: A benign pathway. *Appl. Catal. B* **2021**, *291*, 119974. [CrossRef]

90. Kohlsdorf, A.; Taffa, D.H.; Wark, M. Microwave assisted synthesis of Ta_2O_5 nanostructures for photocatalytic hydrogen production. *J. Photochem. Photobiol. A Chem.* **2018**, *366*, 41–47. [CrossRef]

91. Ravi, P.; Navakoteswara Rao, V.; Shankar, M.; Sathish, M. Heterojunction engineering at ternary $Cu_2S/Ta_2O_5/CdS$ nanocomposite for enhanced visible light-driven photocatalytic hydrogen evolution. *Mater. Today Energy* **2021**, *21*, 100779. [CrossRef]

92. Zhang, L.; Jin, Z.; Tsubaki, N. Activating and optimizing the $MoS_2@MoO_3$ S-scheme heterojunction catalyst through interface engineering to form a sulfur-rich surface for photocatalyst hydrogen evolution. *J. Chem. Eng.* **2022**, *438*, 135238. [CrossRef]

93. Balayeva, N.O.; Fleisch, M.; Bahnemann, D.W. Surface-grafted WO_3/TiO_2 photocatalysts: Enhanced visible-light activity towards indoor air purification. *Catal. Today* **2018**, *313*, 63–71. [CrossRef]

94. Balayeva, N.O.; Zheng, N.; Dillert, R.; Bahnemann, D.W. Visible-light-mediated photocatalytic aerobic dehydrogenation of N-heterocycles by surface-grafted TiO_2 and 4-amino-TEMPO. *ACS Catal.* **2019**, *9*, 10694–10704. [CrossRef]

95. Balayeva, N.O.; Mamiyev, Z.; Dillert, R.; Zheng, N.; Bahnemann, D.W. Rh/TiO_2-Photocatalyzed Acceptorless Dehydrogenation of N-Heterocycles upon Visible-Light Illumination. *ACS Catal.* **2020**, *10*, 5542–5553. [CrossRef]

96. Lin, B.; Ma, B.; Chen, J.; Zhou, Y.; Zhou, J.; Yan, X.; Xue, C.; Luo, X.; Liu, Q.; Wang, J.; et al. Sea-urchin-like ReS_2 nanosheets with charge edge-collection effect as a novel cocatalyst for high-efficiency photocatalytic H_2 evolution. *Chin. Chem. Lett.* **2022**, *33*, 943–947. [CrossRef]

97. Rao, V.N.; Ravi, P.; Sathish, M.; Sakar, M.; Yang, B.L.; Yang, J.M.; Kumari, M.M.; Shankar, M. Titanate quantum dots-sensitized Cu_2S nanocomposites for superficial H_2 production via photocatalytic water splitting. *Int. J. Hydrogen Energy* 2022, *in press*. [CrossRef]

98. Chen, F.; Feng, H.F.; Luo, W.; Wang, P.; Yu, H.G.; Fan, J.J. Simultaneous realization of direct photodeposition and high H_2-production activity of amorphous cobalt sulfide nanodot-modified rGO/TiO_2 photocatalyst. *Rare Met.* **2021**, *40*, 3125–3134. [CrossRef]

99. Yu, B.; Meng, F.; Zhou, T.; Fan, A.; Khan, M.W.; Wu, H.; Liu, X. Construction of hollow TiO_2/CuS nanoboxes for boosting full-spectrum driven photocatalytic hydrogen evolution and environmental remediation. *Ceram. Int.* **2021**, *47*, 8849–8858. [CrossRef]

100. Dong, L.; Wang, P.; Yu, H. EDTA-assisted synthesis of amorphous BiS_x nanodots for improving photocatalytic hydrogen-evolution rate of TiO_2. *J. Alloys Compd.* **2021**, *887*, 161425. [CrossRef]

101. Liu, R.; Fang, S.Y.; Dong, C.D.; Tsai, K.C.; Yang, W.D. Enhancing hydrogen evolution of water splitting under solar spectra using Au/TiO_2 heterojunction photocatalysts. *Int. J. Hydrogen Energy* **2021**, *46*, 28462–28473. [CrossRef]

102. Nguyen, T.T.; Cao, T.M.; Balayeva, N.O.; Pham, V.V. Thermal treatment of polyvinyl alcohol for coupling MoS_2 and TiO_2 nanotube arrays toward enhancing photoelectrochemical water splitting performance. *Catalysts* **2021**, *11*, 857. [CrossRef]

103. Zhang, M.; Zhong, W.; Xu, Y.; Xue, F.; Fan, J.; Yu, H. Photoinduced synthesis of ultrasmall amorphous $NiWS_x$ nanodots for boosting photocatalytic H_2-evolution activity of TiO_2. *J. Phys. Chem. Solids.* **2021**, *149*, 109796. [CrossRef]

104. Dai, X.; Feng, S.; Wu, W.; Zhou, Y.; Ye, Z.; Cao, X.; Wang, Y.; Yang, C. Photocatalytic hydrogen evolution and antibiotic degradation by S-scheme $ZnCO_2S_4/TiO_2$. *Int. J. Hydrogen Energy* **2022**, *47*, 25104–25116. [CrossRef]

105. Qiu, T.; Wang, L.; Zhou, B.; Zhu, Y.; Zhuang, C.; Liu, Q.; Shen, Q.; Xiong, Y.; Zhou, Y.; Zou, Z. Molybdenum Sulfide Quantum Dots Decorated on TiO_2 for Photocatalytic Hydrogen Evolution. *ACS Appl. Nano Mater.* **2022**, *5*, 702–709. [CrossRef]

106. Zuo, G.; Wang, Y.; Teo, W.L.; Xian, Q.; Zhao, Y. Direct Z-scheme TiO_2-$ZnIn_2S_4$ nanoflowers for cocatalyst-free photocatalytic water splitting. *Appl. Catal. B* **2021**, *291*, 120126. [CrossRef]

107. Wang, J.; Fan, Y.; Pan, R.; Hao, Q.; Wu, Y.; van Ree, T.; Holze, R. Regulating Graphitic Carbon Nitride/Cocatalyst by an Amorphous MoS_2 Conformal Multifunctional Intermediate Layer for Photocatalytic Hydrogen Evolution. *ACS Appl. Energy Mater.* **2021**, *4*, 13288–13296. [CrossRef]

108. Mao, L.; Lu, B.; Shi, J.; Zhang, Y.; Kang, X.; Chen, Y.; Jin, H.; Guo, L. Rapid high-temperature hydrothermal post treatment on graphitic carbon nitride for enhanced photocatalytic H_2 evolution. *Catal. Today* 2022, *in press*. [CrossRef]

109. Zhang, Y.; Wan, J.; Zhang, C.; Cao, X. MoS_2 and Fe_2O_3 co-modify g-C_3N_4 to improve the performance of photocatalytic hydrogen production. *Sci. Rep.* **2022**, *12*, 3261. [CrossRef]

110. Wang, J.; Guan, Z.; Huang, J.; Li, Q.; Yang, J. Enhanced photocatalytic mechanism for the hybrid gC_3N_4/MoS_2 nanocomposite. *J. Mater. Chem. A* **2014**, *2*, 7960–7966. [CrossRef]

111. Zhou, J.; Zhang, J.; Zhao, J.; Wang, H.; Liu, R. Accelerated exciton dissociation and electron extraction across the metallic sulfide-carbon nitride ohmic interface for efficient photocatalytic hydrogen production. *J. Mater. Chem. A* **2021**, *9*, 16522–16531. [CrossRef]

112. Wang, M.; Cheng, J.; Wang, X.; Hong, X.; Fan, J.; Yu, H. Sulfur-mediated photodeposition synthesis of NiS cocatalyst for boosting H_2-evolution performance of g-C_3N_4 photocatalyst. *Chin. J. Catal.* **2021**, *42*, 37–45. [CrossRef]

113. Lin, B.; Zhou, Y.; Xu, B.; Zhu, C.; Tang, W.; Niu, Y.; Di, J.; Song, P.; Zhou, J.; Luo, X.; et al. 2D PtS nanorectangles/gC_3N_4 nanosheets with a metal sulfide–support interaction effect for high-efficiency photocatalytic H_2 evolution. *Mater. Horizons* **2021**, *8*, 612–618. [CrossRef] [PubMed]

114. Ding, J.; Song, L.; Li, X.; Chen, L.; Li, X.; Sun, J.; Zhang, X.; Wang, Y.; Tian, X. Interfacial Engineering of the Platinum/Molybdenum Disulfide/graphitic Carbon Nitride Composite for Enhanced Photocatalytic Hydrogen Production. *ACS Appl. Energy Mater.* **2022**, *5*, 8800–8811. [CrossRef]

115. Wei, D.; Liu, Y.; Shao, X.; Zhao, X.; Ghufran, S.; Wang, L.; Wu, R.; Guo, J.; Yang, C. Cooperative effects of zinc–nickel sulfides as a dual cocatalyst for the enhanced photocatalytic hydrogen evolution activity of g-C_3N_4. *J. Environ. Chem. Eng.* **2022**, *10*, 107216. [CrossRef]

116. Lei, W.; Wang, F.; Pan, X.; Ye, Z.; Lu, B. Z-scheme MoO_3-2D SnS nanosheets heterojunction assisted g-C_3N_4 composite for enhanced photocatalytic hydrogen evolutions. *Int. J. Hydrogen Energy* **2022**, *47*, 10877–10890. [CrossRef]

117. Li, J.; Wu, W.; Li, Y.; Zhang, H.; Xu, X.; Jiang, Y.; Lin, K. In Situ Synthesized Rodlike MoS_2 as a Cocatalyst for Enhanced Photocatalytic Hydrogen Evolution by Graphitic Carbon Nitride without a Noble Metal. *ACS Appl. Energy Mater.* **2021**, *4*, 11836–11843. [CrossRef]

118. Li, J.; Cao, W.; Li, Y.; Xu, X.; Jiang, Y.; Lin, K. In Situ Synthesis of Hybrid-Phase WS_2 with S Defects as a Cocatalyst for the g-C_3N_4-Based Photocatalytic Hydrogen Evolution Reaction. *ACS Appl. Energy Mater.* **2022**, *5*, 9463–9470. [CrossRef]

119. Ma, X.; Lei, Z.; Wang, C.; Fu, Z.; Hu, X.; Fan, J.; Liu, E. Fabrication of P-doped Co_9S_8/g-C_3N_4 heterojunction for excellent photocatalytic hydrogen evolution. *Int. J. Hydrogen Energy* **2021**, *46*, 36781–36791. [CrossRef]

120. Wang, C.; Zhang, W.; Fan, J.; Sun, W.; Liu, E. S-scheme bimetallic sulfide $ZnCO_2S_4$/g-C_3N_4 heterojunction for photocatalytic H_2 evolution. *Ceram. Int.* **2021**, *47*, 30194–30202. [CrossRef]

121. Wang, W.; Tao, Y.; Du, L.; Wei, Z.; Yan, Z.; Chan, W.K.; Lian, Z.; Zhu, R.; Phillips, D.L.; Li, G. Femtosecond time-resolved spectroscopic observation of long-lived charge separation in bimetallic sulfide/g-C_3N_4 for boosting photocatalytic H_2 evolution. *Appl. Catal. B* **2021**, *282*, 119568. [CrossRef]

122. Wang, Y.; Hu, Z.; Wang, W.; He, H.; Deng, L.; Zhang, Y.; Huang, J.; Zhao, N.; Yu, G.; Liu, Y.N. Design of well-defined shell-core covalent organic frameworks/metal sulfide as an efficient Z-scheme heterojunction for photocatalytic water splitting. *Chem. Sci.* **2021**, *12*, 16065–16073. [CrossRef]

123. Jin, Z.; Gong, H.; Li, H. Visible-light-driven two dimensional metal-organic framework modified manganese cadmium sulfide for efficient photocatalytic hydrogen evolution. *J. Colloid Interface Sci.* **2021**, *603*, 344–355. [CrossRef] [PubMed]

124. Liu, C.; Liu, Y.; Xiang, Z.; Liu, D.; Yang, Q. Bimetallic MOF-Derived Sulfides with Heterojunction Interfaces Synthesized for Photocatalytic Hydrogen Evolution. *Ind. Eng. Chem. Res.* **2021**, *60*, 11439–11449. [CrossRef]

125. Wang, Y.; Jin, H.; Li, Y.; Fang, J.; Chen, C. Ce-based organic framework enhanced the hydrogen evolution ability of ZnCdS photocatalyst. *Int. J. Hydrogen Energy* **2022**, *47*, 962–970. [CrossRef]

126. Zhang, Q.; Gu, H.; Wang, X.; Li, L.; Zhang, J.; Zhang, H.; Li, Y.F.; Dai, W.L. Robust hollow tubular $ZnIn_2S_4$ modified with embedded metal-organic-framework-layers: Extraordinarily high photocatalytic hydrogen evolution activity under simulated and real sunlight irradiation. *Appl. Catal. B* **2021**, *298*, 120632. [CrossRef]

127. Lian, Z.; Li, Z.; Wu, F.; Zhong, Y.; Liu, Y.; Wang, W.; Zi, J.; Yang, W. Photogenerated hole traps in metal-organic-framework photocatalysts for visible-light-driven hydrogen evolution. *Commun. Chem* **2022**, *5*, 93. [CrossRef]

128. Cao, A.; Zhang, M.; Su, X.; Romanovski, V.; Chu, S. In Situ Fabrication of NiS_2-Decorated Graphitic Carbon Nitride/Metal-Organic Framework Nanostructures for Photocatalytic H_2 Evolution. *ACS Appl. Nano Mater.* **2022**, *5*, 5416–5424. [CrossRef]

129. Ghosh, A.; Karmakar, S.; Rahimi, F.A.; Roy, R.S.; Nath, S.; Gautam, U.K.; Maji, T.K. Confinement Matters: Stabilization of CdS Nanoparticles inside a Postmodified MOF toward Photocatalytic Hydrogen Evolution. *ACS Appl. Mater.* **2022**, *14*, 25220–25231. [CrossRef]

130. Ke, Y.; Zhang, J.; Liu, L.; Li, X.; Liang, Q.; Li, Z. Self-Assembled Zeolitic Imidazole Framework/CdS Hollow Microspheres with Efficient Charge Separation for Enhanced Photocatalytic Hydrogen Evolution. *Inorg. Chem* **2022**, *61*, 10598–10608. [CrossRef]

131. Cheng, L.; Yu, Y.; Huang, R.; Shi, X. Lollipop-shaped Co_9S_8/CdS nanocomposite derived from zeolitic imidazolate framework-67 for the photocatalytic hydrogen production. *Int. J. Hydrogen Energy* **2021**, *46*, 31288–31299. [CrossRef]

132. Xi, X.; Dang, Q.; Wang, G.; Chen, W.; Tang, L. ZIF-67-derived flower-like $ZnIn_2S_4$@CoS_2 heterostructures for photocatalytic hydrogen production. *New J. Chem.* **2021**, *45*, 20289–20295. [CrossRef]

133. Pang, X.; Xue, S.; Zhou, T.; Xu, Q.; Lei, W. 2D/2D nanohybrid of Ti_3C_2 MXene/WO_3 photocatalytic membranes for efficient water purification. *Ceram. Int.* **2022**, *48*, 3659–3668. [CrossRef]

134. Fang, H.; Cai, J.; Li, H.; Wang, J.; Li, Y.; Zhou, W.; Mao, K.; Xu, Q. Fabrication of Ultrathin Two-Dimensional/Two-Dimensional MoS_2/$ZnIn_2S_4$ Hybrid Nanosheets for Highly Efficient Visible-Light-Driven Photocatalytic Hydrogen Evolution. *ACS Appl. Energy Mater.* **2022**, *5*, 8232–8240. [CrossRef]

135. Mamiyev, Z.Q.; Balayeva, N.O. Optical and structural studies of ZnS nanoparticles synthesized via chemical in situ technique. *Chem. Phys. Lett.* **2016**, *646*, 69–74. [CrossRef]

136. Balayeva, N.O.; Askerova, O.O.; Azizov, A.A.; Alosmanov, R.M.; Eyvazova, G.M.; Muradov, M.B. Synthesis of CuS and PbS nanocrystals on the basis of PE/NBR polymer/elastomeric composites for their applications. *Compos. B. Eng.* **2013**, *53*, 391–394. [CrossRef]

137. Guo, J.; Liang, Y.; Liu, L.; Hu, J.; Wang, H.; An, W.; Cui, W. Core-shell structure of sulphur vacancies-CdS@CuS: Enhanced photocatalytic hydrogen generation activity based on photoinduced interfacial charge transfer. *J. Colloid Interface Sci.* **2021**, *600*, 138–149. [CrossRef] [PubMed]

138. Liu, X.; Bie, C.; He, B.; Zhu, B.; Zhang, L.; Cheng, B. 0D/2D NiS/CdS nanocomposite heterojunction photocatalyst with enhanced photocatalytic H_2 evolution activity. *Appl. Surf. Sci.* **2021**, *554*, 149622. [CrossRef]

139. Tian, J.; Xue, W.; Li, M.; Sun, T.; Hu, X.; Fan, J.; Liu, E. Amorphous CoS_x decorated $Cd_{0.5}Zn_{0.5}S$ with a bulk-twinned homojunction for efficient photocatalytic hydrogen evolution. *Catal. Sci. Technol.* **2022**, *12*, 3165–3174. [CrossRef]

140. Liu, S.; Ma, Y.; Chi, D.; Sun, Y.; Chen, Q.; Zhang, J.; He, Z.; He, L.; Zhang, K.; Liu, B. Hollow heterostructure CoS/CdS photocatalysts with enhanced charge transfer for photocatalytic hydrogen production from seawater. *Int. J. Hydrogen Energy* **2022**, *47*, 9220–9229. [CrossRef]

141. Guo, S.; Li, Y.; Xue, C.; Sun, Y.; Wu, C.; Shao, G.; Zhang, P. Controllable construction of hierarchically $CdIn_2S_4$/CNFs/Co_4S_3 nanofiber networks towards photocatalytic hydrogen evolution. *J. Chem. Eng.* **2021**, *419*, 129213. [CrossRef]

142. Zhao, H.; Fu, H.; Yang, X.; Xiong, S.; Han, D.; An, X. MoS_2/CdS rod-like nanocomposites as high-performance visible light photocatalyst for water splitting photocatalytic hydrogen production. *Int. J. Hydrogen Energy* **2022**, *47*, 8247–8260. [CrossRef]

143. Li, P.; Liu, M.; Li, J.; Guo, J.; Zhou, Q.; Zhao, X.; Wang, S.; Wang, L.; Wang, J.; Chen, Y.; et al. Atomic heterojunction-induced accelerated charge transfer for boosted photocatalytic hydrogen evolution over 1D CdS nanorod/2D $ZnIn_2S_4$ nanosheet composites. *J. Colloid Interface Sci.* **2021**, *604*, 500–507. [CrossRef] [PubMed]

144. Bai, J.; Chen, W.; Shen, R.; Jiang, Z.; Zhang, P.; Liu, W.; Li, X. Regulating interfacial morphology and charge-carrier utilization of Ti3C2 modified all-sulfide CdS/$ZnIn_2S_4$ S-scheme heterojunctions for effective photocatalytic H_2 evolution. *J. Mater. Sci. Technol.* **2022**, *112*, 85–95. [CrossRef]

145. Chang, C.J.; Lin, Y.G.; Chen, J.; Huang, C.Y.; Hsieh, S.C.; Wu, S.Y. Ionic liquid/surfactant-hydrothermal synthesis of dendritic PbS@CuS core-shell photocatalysts with improved photocatalytic performance. *Appl. Surf. Sci.* **2021**, *546*, 149106. [CrossRef]

146. Fan, H.T.; Wu, Z.; Liu, K.C.; Liu, W.S. Fabrication of 3D CuS@$ZnIn_2S_4$ hierarchical nanocages with 2D/2D nanosheet subunits p-n heterojunctions for improved photocatalytic hydrogen evolution. *J. Chem. Eng.* **2022**, *433*, 134474. [CrossRef]

147. Li, J.; Li, M.; Jin, Z. Rational design of a cobalt sulfide/bismuth sulfide S-scheme heterojunction for efficient photocatalytic hydrogen evolution. *J. Colloid Interface Sci.* **2021**, *592*, 237–248. [CrossRef] [PubMed]

148. Li, C.; Wang, W.; Yang, Y.; Liu, S.; Zhu, C.; Tian, Q. Core-shell $Cu_{1.94}$S-MnS nanoheterostructures synthesized by cation exchange for enhanced photocatalytic hydrogen evolution. *CrystEngComm* **2021**, *23*, 6291–6299. [CrossRef]

149. Zhou, H.; Xiong, H.; Zhang, R.; Zhang, L.; Zhang, L.; Li, L.; Zhang, W.; Zhu, Z.; Qiao, Z.A. A General Polymer-Oriented Acid-Mediated Self-Assembly Approach toward Crystalline Mesoporous Metal Sulfides. *Small* **2021**, *17*, 2100428. [CrossRef]

150. Mamiyev, Z.; Tzschoppe, M.; Huck, C.; Pucci, A.; Pfnür, H. Plasmon Standing Waves by Oxidation of Si (553)-Au. *J. Phys. Chem. C* **2019**, *123*, 9400–9406. [CrossRef]

151. Himstedt, R.; Rusch, P.; Hinrichs, D.; Kodanek, T.; Lauth, J.; Kinge, S.; Siebbeles, L.D.A.; Dorfs, D. Localized Surface Plasmon Resonances of Various Nickel Sulfide Nanostructures and Au-Ni_3S_2 Core-Shell Nanoparticles. *Chem. Mater.* **2017**, *29*, 7371–7377. [CrossRef]

152. Mamiyev, Z.; Sanna, S.; Ziese, F.; Dues, C.; Tegenkamp, C.; Pfnür, H. Plasmon Localization by H Induced Band Switching. *J. Phys. Chem. C* **2019**, *124*, 958–967. [CrossRef]

153. Mamiyev, Z.; Tegenkamp, C.; Pfnür, H. Plasmon localization by adatoms in gold atomic wires on Si (775). *J. Phys. Condens. Matter* **2021**, *33*, 205001. [CrossRef] [PubMed]

154. Faucheaux, J.A.; Stanton, A.L.D.; Jain, P.K. Plasmon Resonances of Semiconductor Nanocrystals: Physical Principles and New Opportunities. *J. Phys. Chem. Lett.* **2014**, *5*, 976–985. [CrossRef] [PubMed]

155. Mamiyev, Z.; Fink, C.; Holtgrewe, K.; Pfnür, H.; Sanna, S. Enforced Long-Range Order in 1D Wires by Coupling to Higher Dimensions. *Phys. Rev. Lett.* **2021**, *126*, 106101. [CrossRef]

156. Ingram, D.B.; Linic, S. Water Splitting on Composite Plasmonic-Metal/Semiconductor Photoelectrodes: Evidence for Selective Plasmon-Induced Formation of Charge Carriers near the Semiconductor Surface. *J. Am. Chem. Soc.* **2011**, *133*, 5202–5205. [CrossRef]

157. Chen, W.B.; Hu, L.Y.; Meng, F.; Tang, L.; Liang, S.; Li, J.B. Dual-plasmon-induced photocatalytic performance enhancement in Au-PbS-CdS nanodumbbells with double Au caps on the ends. *Opt. Mater.* **2021**, *117*, 111210. [CrossRef]

158. Liu, Y.T.; Lu, M.Y.; Perng, T.P.; Chen, L.J. Plasmonic enhancement of hydrogen production by water splitting with CdS nanowires protected by metallic TiN overlayers as highly efficient photocatalysts. *Nano Energy* **2021**, *89*, 106407. [CrossRef]

159. Tu, C.Y.; Wu, J.M. Localized surface plasmon resonance coupling with piezophototronic effect for enhancing hydrogen evolution reaction with Au@MoS_2 nanoflowers. *Nano Energy* **2021**, *87*, 106131. [CrossRef]

160. Yang, J.L.; He, Y.L.; Ren, H.; Zhong, H.L.; Lin, J.S.; Yang, W.M.; Li, M.D.; Yang, Z.L.; Zhang, H.; Tian, Z.Q.; et al. Boosting Photocatalytic Hydrogen Evolution Reaction Using Dual Plasmonic Antennas. *ACS Catal.* **2021**, *11*, 5047–5053. [CrossRef]

161. Cheng, C.; Zhang, J.; Zeng, R.; Xing, F.; Huang, C. Schottky barrier tuning via surface plasmon and vacancies for enhanced photocatalytic H_2 evolution in seawater. *Appl. Catal. B* **2022**, *310*, 121321. [CrossRef]

162. Mandari, K.K.; Son, N.; Kim, Y.S.; Kang, M. Plasmonic quaternary heteronanostructures (HNSs) for improved solar light utilization, spatial charge separation, and stability in photocatalytic hydrogen production. *J. Colloid Interface Sci.* **2021**, *582*, 720–731. [CrossRef]

163. Liu, X.; Wang, S.; Yang, F.; Zhang, Y.; Yan, L.; Li, K.; Guo, H.; Yan, J.; Lin, J. Construction of $Au/g-C_3N_4/ZnIn_2S_4$ plasma photocatalyst heterojunction composite with 3D hierarchical microarchitecture for visible-light-driven hydrogen production. *Int. J. Hydrogen Energy* **2022**, *47*, 2900–2913. [CrossRef]

164. Ren, B.; Luan, Q.; Ma, L.; Ding, Y.; Ma, D.; Cao, X.; Guo, Y.; Guan, R.; Chen, Q. Amorphous domain induced LSPR Zn-Cr-In-S solid solution with enhanced visible photocatalytic H_2 production. *Mater. Chem. Phys.* **2022**, *285*, 126100. [CrossRef]

165. Simon, T.; Carlson, M.T.; Stolarczyk, J.K.; Feldmann, J. Electron Transfer Rate vs Recombination Losses in Photocatalytic H_2 Generation on Pt-Decorated CdS Nanorods. *ACS Energy Lett.* **2016**, *1*, 1137–1142. [CrossRef]

166. Xue, W.; Sun, H.; Hu, X.; Bai, X.; Fan, J.; Liu, E. UV-VIS-NIR-induced extraordinary H_2 evolution over $W_{18}O_{49}/Cd_{0.5}Zn_{0.5}S$: Surface plasmon effect coupled with S-scheme charge transfer. *Chin. J. Catal.* **2022**, *43*, 234–245. [CrossRef]

167. Zhong, W.; Wu, X.; Liu, Y.; Wang, X.; Fan, J.; Yu, H. Simultaneous realization of sulfur-rich surface and amorphous nanocluster of NiS_{1+x} cocatalyst for efficient photocatalytic H_2 evolution. *Appl. Catal. B* **2021**, *280*, 119455. [CrossRef]